Active Janus colloids at chemically structured surfaces

Cite as: J. Chem. Phys. **150**, 204904 (2019); https://doi.org/10.1063/1.5091760
Submitted: 05 February 2019 • Accepted: 02 May 2019 • Published Online: 30 May 2019

W. E. Uspal, M. N. Popescu, S. Dietrich, et al.

The Journal of Chemical Physics ARTICLE scitation.org/journal/jcp

Active Janus colloids at chemically structured surfaces

Cite as: J. Chem. Phys. 150, 204904 (2019); doi: 10.1063/1.5091760
Submitted: 5 February 2019 • Accepted: 2 May 2019 •
Published Online: 30 May 2019 Corrected: 2 August 2019

W. E. Uspal,[1] M. N. Popescu,[2] S. Dietrich,[2] and M. Tasinkevych[3,a)]

AFFILIATIONS

[1] Department of Mechanical Engineering, University of Hawai'i at Mānoa, 2540 Dole Street, Holmes Hall 302, Honolulu, Hawaii 96822, USA
[2] Max-Planck-Institut für Intelligente Systeme, Heisenbergstr. 3, D-70569 Stuttgart, Germany and IV. Institut für Theoretische Physik, Universität Stuttgart, Pfaffenwaldring 57, D-70569 Stuttgart, Germany
[3] Departamento de Física, Faculdade de Ciências, Universidade de Lisboa, Campo Grande P-1749-016 Lisboa, Portugal and Centro de Física Teórica e Computacional, Universidade de Lisboa, Campo Grande P-1749-016 Lisboa, Portugal

Note: This article is part of the Special Topic "Chemical Physics of Active Matter" in J. Chem. Phys.
[a)] **Author to whom correspondence should be addressed:** mtasinkevych@fc.ul.pt

ABSTRACT

If catalytically active Janus particles are dispersed in certain liquid solutions, they can create a gradient in the chemical composition of this solution along their surfaces, as well as along any nearby confining surfaces. This gradient drives self-propulsion via a self-phoretic mechanism, while the compositional gradient along a wall gives rise to chemiosmosis, which additionally contributes to self-motility. In this study, we analyze theoretically the dynamics of an active colloid near chemically patterned walls. We use a point-particle approximation combined with a multipole expansion in order to discuss the effects of pattern geometry and chemical contrast on the particle trajectories. In particular, we consider planar walls patterned with chemical steps and stripes. We investigate in detail the changes in the topology of the corresponding phase portraits upon varying the chemical contrast and the stripe width.

I. INTRODUCTION

Active colloidal particles can perform autonomous directional motion within a liquid medium.[1–7] This offers the possibility to use such particles as autonomous micromotors, which perform useful tasks such as delivering drugs, sensing a specific substance, or assembling structures via the autonomous local deposition of materials.[8–11] Catalytic colloids form a large class of active particles which employ self-phoretic effects[6,7,12–16] for their motion. For example, a colloidal particle partially covered by a catalyst will activate a chemical reaction in the surrounding solution.[1,2,13,17] This, in turn, will generate gradients of solute concentration or of an electric potential, leading to a directed motion of the particle by self-diffusiophoretic[13,14,18] or self-electrophoretic[7,16,19–21] mechanisms, respectively. Another distinct class of active particles is formed by gold-capped Janus colloidal spheres which are suspended in near-critical fluids such as water-lutidine mixtures.[22] These particles can perform active Brownian motion when illuminated by light. The particle motion has been attributed to self-thermophoresis,[15] self-diffusiophoresis,[23] or self-phoresis due to a local solvent demixing, and associated self-generated chemical potential gradients.[24]

Most of the experiments carried out so far have used Pt catalyzed[2,3,13,17] decomposition of hydrogen peroxide into water and oxygen. Self-propelled particles frequently employed in experiments are, e.g., gold-platinum nanorods[1,3] or silica particles partially coated by a catalyst.[8,13,25,26] Theoretically, aside from using molecular dynamics (MD) simulations,[27–31] mesoscopic continuum approaches have been employed,[12,14,18] based on the classical theory of diffusiophoresis.[32,33] Using this method, the dependence of the self-propulsion velocity on the shape and surface chemistry of microswimmers,[18,34–36] their chemotactic behavior,[37,38] and how active colloids can be used as cargo carriers[26,39] have been studied.

A few recent studies have begun to address self-phoresis in bounded systems. In Ref. 29, MD simulations have been used to study self-diffusiophoresis within a square channel. For a highly idealized confining geometry, an increase in the self-diffusiophoretic velocity was predicted theoretically in Ref. 40. The role of the boundaries was also highlighted in Ref. 26, where the motion of carrier-cargo composites has been studied near a single wall. Translocation of a Janus active particle through cylindrical pores has been addressed in Ref. 41, which reported a decrease in the particle velocity induced by the confinement and emphasized the importance of the "chemical effects" in addition to the "standard" hydrodynamic interaction. Experimentally, wall-bounded motion of active Janus particles was observed in Refs. 20 and 42. Theoretical models based on a far-field multipole description of the microswimmers[43] or models, in which the surface slip is specified *a priori*,[44] showed that the hydrodynamic interaction may generate particle-wall attraction and sliding steady states along the wall.[44] However, as shown recently,[45–47] a more realistic description, explicitly taking into account the propulsive mechanism, is required to fully understand the particle dynamics near boundaries. Indeed, novel sliding and hovering steady states were predicted in Refs. 45 and 48–50 for a Janus microswimmer near a wall by numerically solving the coupled hydrodynamic transport equations for chemical fluxes and momentum.

The sliding states may be exploited further in order to achieve desired particle behaviors in two-dimensional (2D) space by, e.g., endowing the confining surface either with topographical or chemical contrasts. For example, the occurrence of wall-bounded sliding states explains experimentally reported directional guidance of chemically active microswimmers by shallow steplike topographical features.[46] In the case of chemically patterned walls, it was shown recently[51,52] that under certain conditions a stable motion along a one-dimensional (1D), macroscopically long chemical stripe may be obtained.

More specifically, Ref. 51 demonstrates that (i) a catalyst-forward spherical particle can robustly follow certain chemical stripes; (ii) an inert-forward spherical particle can achieve a motionless docking steady state at a chemical step with sufficiently strong chemical contrast. This proof of concept study employed, for illustration only, a single realization of the chemical step (i.e., only one value of the chemical contrast between the right and the left side of the surface), a single realization of the chemical stripe (i.e., one value of the chemical contrast between the two chemical entities of the surface), and a single value of the distance between the particle and the surface. Additionally, since Ref. 51 is focused on the bare possibility of guided motion, it does not systematically explore the very rich landscape of other dynamical behaviors, e.g., reflection from a chemical step, or focusing off the particle orientation as a particle crosses a step. Reference 52 discusses in detail the effect of the particle shape on the dynamics of active, half-covered spherocylinders at chemical steps and stripes. The guiding of catalytic sphere-dimer nanoparticles by highly idealized chemical stripes has been reported in Ref. 53 based on using the hybrid molecular dynamics multiparticle collision dynamics method.

In this study, we further explore this idea of controlling the motion of Janus microswimmers via chemically structured, planar surfaces. By using the analytical method developed in Ref. 51, here we address the following questions: (i) How does the dynamics of an active Janus colloid depend on the chemical contrast between the right and the left side of the chemical step and on the particle-surface separation? In particular, we want to understand how the topology of the phase portrait [in the (x_p, ϕ) plane, see Fig. 1(b)] depends on the aforementioned parameters. (ii) Concerning a self-propelled particle at a chemical stripe, how does this phase portrait depend on the chemical contrast of the stripe and on the particle-surface separation? (iii) In general, what dynamical behaviors can be found beyond stripe-guided or step-guided motion?

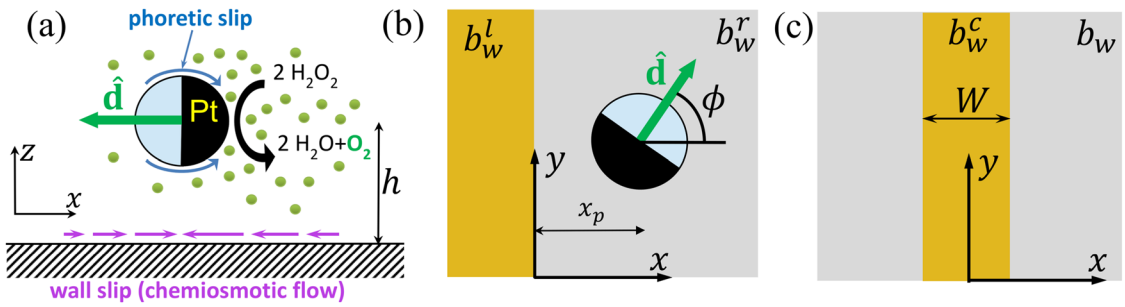

FIG. 1. (a) A catalytic Janus sphere above a planar wall at height h. The black region on the particle indicates the catalytic cap which emits solute molecules (green discs, O_2) at a constant rate per area κ. The solute molecules interact with the colloidal particle, and due to the inhomogeneous solute distribution, a gradient of osmotic pressure emerges in the direction parallel to the surface (for the orientation $\hat{\mathbf{d}}$ shown) which drives a surface flow as indicated by two blue arrows. The direction of the surface flow corresponds to the repulsive nature of the solute-particle interaction, resulting in an inert-forward self-diffusiophoretic motion in direction $\hat{\mathbf{d}}$. If the solute-particle interaction is attractive, the flow is away from the cap, leading to catalyst-forward motion in direction $-\hat{\mathbf{d}}$. The solute gradient also drives chemiosmotic flow at the wall, schematically indicated by purple lines, assuming a repulsive nature of the solute-wall interaction. (b) Schematic top-down view of a Janus particle above a chemically patterned substrate. The gray region, which is characterized by the surface phoretic mobility b_w^r, is more repulsive for the solute than the orange one with the surface phoretic mobility b_w^l. The orientation vector $\hat{\mathbf{d}}$ and the x-axis form the angle ϕ; x_p is the distance between the chemical step and the particle center. (c) A top-down view of the wall patterned with a rectangular chemical stripe (orange) of width W. The stripe extends in the y-direction and carries the surface phoretic mobility b_w^c. The rest of the wall (gray) exhibits the surface phoretic mobility b_w.

The paper is organized as follows: In Sec. II, we present our theoretical approach which is based on the so-called point-particle approximation and a multipole expansion for the concentration of the reaction product in the solution. Concerning some of the material of this section, we also refer to the supplementary material of Ref. 51, parts of which are also presented in Appendixes A–C. In Secs. III–V, we describe and discuss our results. For the case of a chemical step, we show how changing the chemical contrast of the substrate affects the topology of the corresponding phase portraits for both inert-forward and catalyst-forward Janus colloids. It is demonstrated that inert-forward particles can dock at the boundary between the two regions of the substrate forming a chemical step and the conditions for docking to occur are identified. In the case of a chemical stripe, only catalyst-forward microswimmers are considered because only such particles can stably follow a chemical stripe (see Ref. 51). Finally, in Sec. VI, we summarize our findings.

II. MODEL AND THEORETICAL APPROACH

Assuming a stationary reference frame in which the instantaneous position of the Janus particle is $\mathbf{x}_0 = (x_p, y_p, h)$, we consider an impermeable spherical colloid of radius R with a caplike region covered by a catalyst, which promotes the chemical reaction in the surrounding solution, as schematically depicted in Fig. 1. The orientation $\hat{\mathbf{d}}$ of the particle is directed along the axis of symmetry from the catalytic region to the particle center (Fig. 1). In this study, we focus on the particular case in which the net result of the chemical reaction can be approximated as the generation of a solute, i.e., the catalytic cap acts effectively as an emitter of the solute, and in which the reaction does not lead to solvent depletion near the catalytic cap. This scenario corresponds approximately to Pt-catalyzed decomposition of hydrogen peroxide (in aqueous solution) into water and oxygen,[13,54] where oxygen plays the role of the product (solute) and the solvent is a binary liquid mixture of H_2O and H_2O_2, altogether forming a solution.

Nonsymmetric coverage of the particle by the catalyst, acting as a source of solute, gives rise to a nonuniform and time dependent composition of the solution, which is, in general, characterized by the solute (O_2) number density $c(\mathbf{x}, t)$. We assume that the Péclet number $Pe \equiv U_0 R/D$, where U_0 is a characteristic velocity of the particle with radius R and D is the diffusion coefficient of the solute molecule (O_2), is small such that the convection of the solute molecules can be disregarded compared to its diffusive transport. Consequently, at each instantaneous position of the particle, the solute number density can attain its steady-state, which is governed by the Laplace equation $\nabla^2 c = 0$. We assume that $c(|\mathbf{x}| \to \infty) = 0$ and employ the following boundary conditions at the particle surface with outward normal $\hat{\mathbf{n}}$:

$$-D\,\hat{\mathbf{n}} \cdot \nabla c = \begin{cases} \kappa, & \mathbf{x}_s \in \text{catalytic cap}, \\ 0, & \mathbf{x}_s \in \text{inert face}, \end{cases}$$

where κ is a constant rate per area of the emission of the solute and $\mathbf{x}_s$ is the location on the surface. At the planar wall placed at $z = 0$, we impose the no-flux boundary condition $\hat{\mathbf{z}} \cdot \nabla c = 0$, where $\hat{\mathbf{z}}$ is the surface normal pointing into the solution.

According to the classical theory of neutral diffusiophoresis,[33] the nonuniform solute number density $c(\mathbf{x})$ gives rise to lateral gradients of the osmotic pressure along the surface of the particle as well as along the surface of the confining wall. The lateral gradient, which is concentrated only within a thin interfacial layer of molecular thickness, drives interfacial flow around the particles and along the surface of the wall, which are accounted for as an effective slip boundary condition $\mathbf{v}_s(\mathbf{x}_s) = -b(\mathbf{x}_s)\nabla_{||} c$ for the outer hydrodynamic flow (i.e., outside of the diffuse interfacial region). $\nabla_{||}$ denotes the projection of the gradient operator onto the corresponding local tangential plane of the surface of the particle or the wall, and $b(\mathbf{x}_s)$ is a material dependent parameter which encapsulates the details of the effective solute-surface interactions.

Furthermore, we assume that for typical velocities U_0 in self-phoresis the Reynolds number obeys $Re \equiv \rho U_0 R/\eta \ll 1$, where ρ and η are the mass density and the viscosity, respectively, of the solution. With this the flow field $\mathbf{u}(\mathbf{x})$ and the pressure field $P(\mathbf{x})$ in the outer region satisfy the incompressible, force free Stokes equations

$$-\nabla P + \eta \nabla^2 \mathbf{u} = 0 \tag{1}$$

and

$$\nabla \cdot \mathbf{u} = 0, \tag{2}$$

subject to the boundary conditions

$$\mathbf{u}(\mathbf{x}_s) = \begin{cases} \mathbf{U} + \boldsymbol{\Omega} \times (\mathbf{x}_s - \mathbf{x}_0) + \mathbf{v}_s(\mathbf{x}_s), & \mathbf{x}_s \in \text{on the particle}, \\ \mathbf{v}_s(\mathbf{x}_s), \mathbf{x}_s \in \text{on the wall}, \\ \mathbf{0}, |\mathbf{x}_s| \to \infty. \end{cases} \tag{3}$$

In the above equations, $\mathbf{U}$ and $\boldsymbol{\Omega}$ are unknown translational and angular velocities of the particle, respectively, which are determined by imposing that the particle is force- and torque-free. Exploiting the linearity of Eqs. (1)–(3), we make the ansatz $\mathbf{U} = \mathbf{U}^{ws} + \mathbf{U}^{sd}$ and $\boldsymbol{\Omega} = \boldsymbol{\Omega}^{ws} + \boldsymbol{\Omega}^{sd}$, where the superscripts indicate the respective velocity contributions stemming from *w*all *s*lip and *s*elf-*d*iffusiophoresis (particle slip). Physically, $\mathbf{U}^{ws}$ and $\boldsymbol{\Omega}^{ws}$ originate in the chemiosmotic flows induced at the surface of the confining wall by the gradient of the solute concentration. These interfacial flows drive flow in the bulk solution, coupling back to the particle and affecting its motion.

The quantities $\mathbf{U}^{sd}$ and $\boldsymbol{\Omega}^{sd}$ in the presence of an inert uniform wall have been studied in detail in Ref. 45, where it was shown that $\mathbf{U}^{sd}$ depends only on h and $\hat{\mathbf{d}} \cdot \hat{\mathbf{z}}$. Therefore, in order to simplify the analysis, we restrict $\hat{\mathbf{d}}$ to the x–y plane ($\hat{\mathbf{d}} \cdot \hat{\mathbf{z}} = 0$) and take h to be constant. In principle, such wall-bounded 2D motion may also be achieved by using magnetic fields and particles containing a magnetic core.[8] In the following, we set $\mathbf{U}^{sd} = U^{sd}\hat{\mathbf{d}}$, with U^{sd} treated as an input parameter. We recall that for $U^{sd} > 0$ ($U^{sd} < 0$), the particle moves away from (toward) its cap when it is in the bulk fluid due to the repulsive (attractive) interaction between the particle and the solute.[33] Additionally, by symmetry, one has $\Omega_z^{sd} = 0$. The trajectory of the particle is obtained by numerical integration of the coupled equations

$$\begin{aligned} \dot{x}_p &= U^{sd}\cos(\phi) + U_x^{ws}(x_p, \phi), \\ \dot{y}_p &= U^{sd}\sin(\phi) + U_y^{ws}(x_p, \phi), \end{aligned} \tag{4}$$

and

$$\dot{\phi} = \Omega_z^{ws}(x_p, \phi). \tag{5}$$

We calculate $\mathbf{U}^{ws}$ and $\mathbf{\Omega}^{ws}$ by employing the Lorentz reciprocal theorem, expressed in Eq. (A1).[55] The details of these calculations are provided in Appendix A. As the "unprimed" problem, we chose the one for the six unknowns $\mathbf{V} \equiv (\mathbf{U}^{ws}, \mathbf{\Omega}^{ws})$, requiring six "primed" subproblems. For the primed subproblems $(\mathbf{u}'^{(j)}, \boldsymbol{\sigma}'^{(j)})$, indexed by j, we consider a passive colloid subject to an external normalized force in the $\hat{x}$, $\hat{y}$, or $\hat{z}$ direction for $j = 1, 2, 3$, or an external normalized torque in the $\hat{x}$, $\hat{y}$, or $\hat{z}$ direction for $j = 4, 5, 6$. For each of the cases $j = 1, \ldots, 6$, we impose no-slip boundary conditions at the planar wall and $\mathbf{u}'^{(j)} = 0$ at infinity. At the particle surface, there is a no-slip condition $\mathbf{u}'^{(j)} = \mathbf{U}'^{(j)} + \mathbf{\Omega}'^{(j)} \times (\mathbf{x} - \mathbf{x}_0)$, where $\mathbf{U}'^{(j)}$ and $\mathbf{\Omega}'^{(j)}$ are the translational and angular velocities, respectively, of the particle driven by the external force or the external torque in subproblem j. The expressions for the fluid stresses $\boldsymbol{\sigma}'^{(j)}$ and for the velocity field $\mathbf{u}'^{(j)}$ $(j = 1, \ldots, 6)$ of the auxiliary solution of the Stokes equation (required by the Lorentz theorem) are provided in Appendix B. Finally, the approximation used for determining $c(\mathbf{x}_s)$, which, in turn, is needed to calculate the phoretic slip boundary conditions $\mathbf{v}_s(\mathbf{x}_s) = -b_w(\mathbf{x}_s)\nabla_{\|}c(\mathbf{x}_s)$, is presented in Appendix C.

Taking into account only the contributions of the monopole (^{mp}) and dipole (^{dp}) terms of the number density [see Eqs. (C3) and (C5)] to the particle velocity, we write $\mathbf{U}^{ws} \approx \mathbf{U}^{mp} + \mathbf{U}^{dp}$ and $\mathbf{\Omega}^{ws} \approx \mathbf{\Omega}^{mp} + \mathbf{\Omega}^{dp}$. Because of the assumption that the self-propulsion proceeds in the x–y plane, only the components U_x, U_y, and Ω_z are of interest here, corresponding to the components V_1, V_2, and V_6 of the generalized velocity $\mathbf{V}$. Below, the monopole and dipole contributions to these velocity components are calculated for a homogeneous substrate, a chemical step, and a chemical stripe. In each case, the components of the stress tensor $\boldsymbol{\sigma}'^{(j)}|_{z=0}$ required for the calculation of U_x $(j = 1)$, U_y $(j = 2)$, and Ω_z $(j = 6)$ are provided by Eqs. (B5), (B6), and (B12), respectively.

III. SURFING ABOVE A UNIFORM SUBSTRATE

For a uniform substrate with surface mobility b_w, Eq. (A4) yields

$$V_j = b_w \int_{-\infty}^{-\infty} dx \int_{-\infty}^{\infty} dy \left(\nabla_{\|}c \cdot \boldsymbol{\sigma}'^{(j)} \cdot \hat{\mathbf{z}}\right)|_{z=0}. \tag{6}$$

The monopole contributions are obtained by replacing $\nabla_{\|}c$ in Eq. (6) with the corresponding expression in Eq. (C3). The result is

$$U_x^{mp} = U_y^{mp} = 0, \Omega_z^{mp} = 0. \tag{7}$$

This result is expected because in the plane of the wall the number density distribution due to a monopole above the wall is radially symmetric around (x_p, y_p). Therefore, the flow it induces cannot drive translations parallel to the plane or in-plane rotations of $\hat{\mathbf{d}}$. Similarly, the dipole contributions are obtained by replacing $\nabla_{\|}c$ in Eq. (6) by the corresponding expression in Eq. (C5). After carrying out the ensuing integrals, we obtain

$$U_x^{dp} = -\frac{b_w R^3 |\alpha_1|}{16Dh^3}\cos(\phi), \tag{8}$$

$$U_y^{dp} = -\frac{b_w R^3 |\alpha_1|}{16Dh^3}\sin(\phi), \tag{9}$$

and

$$\Omega_z^{dp} = 0, \tag{10}$$

with $\alpha_1 = -3\kappa/4$ [see Eq. (C1)], where ϕ is the angle between $\hat{\mathbf{d}}$ and $\hat{\mathbf{x}}$. Accordingly, these results show that, above a uniform substrate, the dipole contribution drives chemiosmotic "surfing," i.e., translation in the $-\mathrm{sgn}(b_w)\hat{\mathbf{d}}$ direction: $\mathbf{U}^{dp} = -\frac{b_w R^3|\alpha_1|}{16Dh^3}\hat{\mathbf{d}}$.

We note that "surfing" can change the inert-forward or catalyst-forward character of the motion in direction $\hat{\mathbf{d}}$ near a surface as compared with that observed in the bulk; here, the bulk motion is represented by the parameter U^{sd}. For such a change to occur, one must have $|b_w| \gg |b_p|$, where $b(\mathbf{x}_s) = b_p$ at the particle surface; we recall that $U^{sd} \propto b_p$. The occurrence of this special case requires that the particle and substrate materials have very distinct strengths of interaction with the solute.

IV. CHEMICAL STEPS

We first consider a wall with a chemical step between two materials such that $b(\mathbf{x}_s) = b_w^l$ for $x < 0$ and $b(\mathbf{x}_s) = b_w^r$ for $x > 0$. We introduce $\zeta \equiv b_w^r/b_w^l$ in order to quantify the strength of the chemical contrast between two regions of the wall. Accordingly, Eq. (A4) is evaluated piecewise

$$V_j = b_w^l \int_{-\infty}^{0} dx \int_{-\infty}^{\infty} dy \left(\nabla_{\|}c \cdot \boldsymbol{\sigma}'^{(j)} \cdot \hat{\mathbf{z}}\right) + b_w^r \int_{0}^{\infty} dx \int_{-\infty}^{\infty} dy \left(\nabla_{\|}c \cdot \boldsymbol{\sigma}'^{(j)} \cdot \hat{\mathbf{z}}\right). \tag{11}$$

Following the line of the derivations in Subsection III, after straightforward but cumbersome algebra, we obtain the contributions from the monopole term,

$$U_x^{mp} = \frac{3hR^2\alpha_0}{16D}\frac{(b_w^r - b_w^l)(h^2 + 2x_p^2)}{(h^2 + x_p^2)^{5/2}} \tag{12}$$

{with $\alpha_0 = \kappa/2$ [see Eq. (C1)]} and

$$U_y^{mp} = 0, \Omega_z^{mp} = 0, \tag{13}$$

and from the dipole term,

$$U_x^{dp} = \frac{|\alpha_1|R^3}{256Dh^3}\left[-8(b_w^r + b_w^l) + (b_w^l - b_w^r) \times \frac{(-25\,h^4 + 28h^2x_p^2 + 8x_p^4)x_p^3}{(h^2 + x_p^2)^{7/2}}\right]\cos(\phi), \tag{14}$$

$$U_y^{dp} = \frac{|\alpha_1|R^3}{256Dh^3}\left[-8(b_w^r + b_w^l) + (b_w^l - b_w^r) \times \frac{(8x_p^4 + 20h^2x_p^2 + 3h^4)x_p}{(h^2 + x_p^2)^{5/2}}\right]\sin(\phi), \tag{15}$$

and

$$\Omega_z^{dp} = -\frac{3hR^3|\alpha_1|}{64D}\frac{(b_w^l - b_w^r)}{(h^2 + x_p^2)^{5/2}}\sin(\phi). \quad (16)$$

As expected, the results do not depend on y_p because the system exhibits translational symmetry along the y-direction. We emphasize that Ω_z^{dp} is mirror symmetric with respect to $x_p = 0$, which is a general property of Ω_z^{ws}, valid for any contribution from higher multipole moments.[51] It turns out that precisely the same arguments can be applied to U_x^{mp} in order to infer that it is an even function of x_p. Further details are provided in Appendix D. The x-component of the monopole term U_x^{mp} vanishes for $|x_p| \to \infty$, while $\lim_{x_p\to+\infty} U_x^{dp} = -|\alpha_1|R^3 b_w^r \cos(\phi)/(16Dh^3) \neq 0$ and $\lim_{x_p\to-\infty} U_x^{dp} = -|\alpha_1|R^3 b_w^l \cos(\phi)/(16Dh^3) \neq 0$, i.e., the particle "senses" an approximately uniform surface beneath itself. This asymptotic expression coincides with the one in Eq. (8) giving the dipole contribution at a uniform surface.

Figure 2 reports on $U_x^{ws} \simeq U_x^{mp} + U_x^{dp}$ at fixed orientations $\phi = 0°$ [Fig. 2(a)] and $\phi = 180°$ [Fig. 2(b)], as well as on $U_y^{ws} \simeq U_y^{dp}$ [Fig. 2(c)] and on Ω_z^{dp} [Fig. 2(d)], both at fixed orientation $\phi = 90°$, as functions of x_p. The velocities are presented in units of $U_0 \equiv 2|b_w^l|\alpha_0/D$. The leading order monopole contribution always drives translation of the particle toward that side of the wall which exhibits the larger value of b_w, which in the present case is the left (less repulsive) side. The motion away from the step {i.e., $U_x^{ws} > 0$ as observed for $x_p > 0$ and at $\phi = 0°$ [Fig. 2(a)]} is due to the dipole term in Eq. (14), which is independent of x_p. Furthermore, the dipole contribution to the angular velocity in Eq. (16) drives *rotation* of the catalytic cap of the particle toward the side of the wall with the larger value of b_w (i.e., the left, less repulsive side).

A. Phase portraits in the (ϕ, x_p) plane for inert-forward colloids

Figure 3 reports the effects of the chemical contrast ζ at fixed $U^{sd} = (\mathbf{U}^{sd}\cdot\hat{\mathbf{d}}) > 0$ (inert-forward) on the topology of the phase portraits in the (ϕ, x_p) plane. We assume that $b_w^r < b_w^l < 0$. For strong enough chemical contrast, we find that inert-forward particles can dock at the chemical step. The corresponding stable fixed points are depicted in Figs. 3(a), 3(b), and 3(d) as white triangles. The *d*ocking occurs at $x_p = x_p^d < 0$ and $\phi = 0°$, i.e., the particle is stationary above the left (i.e., less repulsive) side of the surface, with $\hat{\mathbf{d}}$ perpendicular to the chemical step. The dependence of x_p^d on $\zeta > 0$ is shown in Fig. 4 by red lines representing various values of the separation h between the colloid center and the wall. The black curves in Fig. 4 show the dependence on ζ of the location of the saddle fixed points, indicated as white circles in Figs. 3(a), 3(b), and 3(d). At a certain value of $\zeta > 0$, the two fixed points collide and "annihilate" each other [see Fig. 3(c)]. The location of this bifurcation point, as a function of ζ, may be tuned by varying h.

The docking state results from the interplay between the dipolar rotation term Ω_z^{dp} [Eq. (16)] and the sum of the monopole term U_x^{mp} [Eq. (12)] and the self-diffusiophoresis contribution $\mathbf{U}^{sd}$. The rotation induced by the chemical step orients the particle at $\phi = 0°$ such that the black cap completely faces the region of weaker repulsion (orange region in Fig. 1). With this orientation, U_x^{mp} drives the particle away from the step into the orange region, while $\mathbf{U}^{sd}$ is directed toward the step. At a certain condition, the three contributions balance each other, leading to the motionless docking state. As a condition for docking, we identify the relation $U_x^{tot} \equiv U_x^{sd} + U_{x0}^{mp} + U_{x0}^{dp} \lesssim 0$, which implies that the particle cannot cross the step; U_{x0}^{mp} and U_{x0}^{dp} are the monopole [Eq. (12)] and dipole [Eq. (14)] contributions, respectively, to U_x^{ws} at $x_p = 0$, and $U_x^{sd} = U^{sd}\cos(\phi)$, with U^{sd}

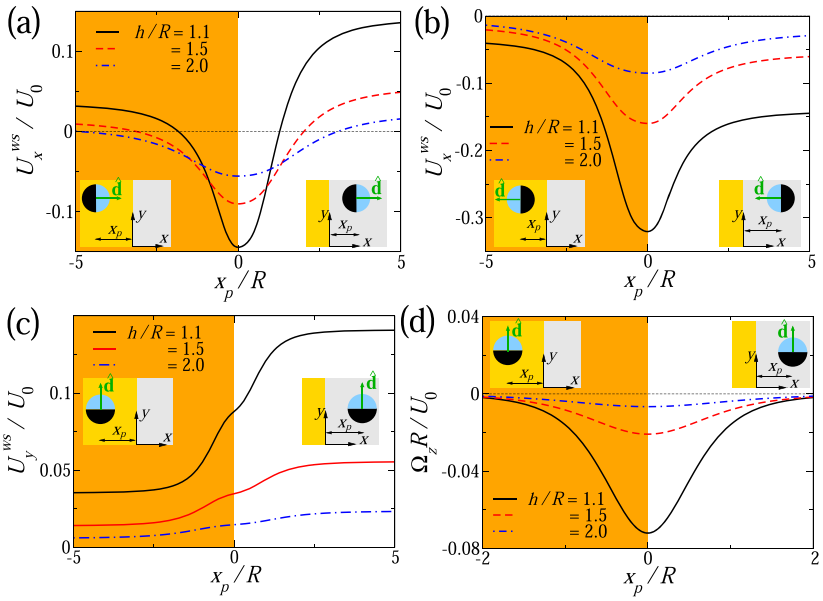

FIG. 2. [(a) and (b)] Chemiosmotic contribution $U_x^{ws} \simeq U_x^{mp} + U_x^{dp}$ [see Eqs. (12) and (14)] to the particle translational velocity in the x-direction as a function of x_p for particle orientation $\phi = 0°$ and $\phi = 180°$, respectively. (c) Chemiosmotic contribution $U_y^{ws} \simeq U_y^{dp}$ [see Eq. (15)] to the particle translational velocity in the y-direction as a function of x_p for a particle oriented parallel ($\phi = 90°$) to the chemical step. (d) Angular velocity, calculated from Eq. (16) of a particle oriented parallel ($\phi = 90°$) to the chemical step as a function of x_p. The results are obtained for $b_w^r/b_w^l = 4$, $b_w^l < 0$, and are presented in units of $U_0 \equiv 2|b_w^l|\alpha_0/D$. The two regions of the chemical step are color-coded.

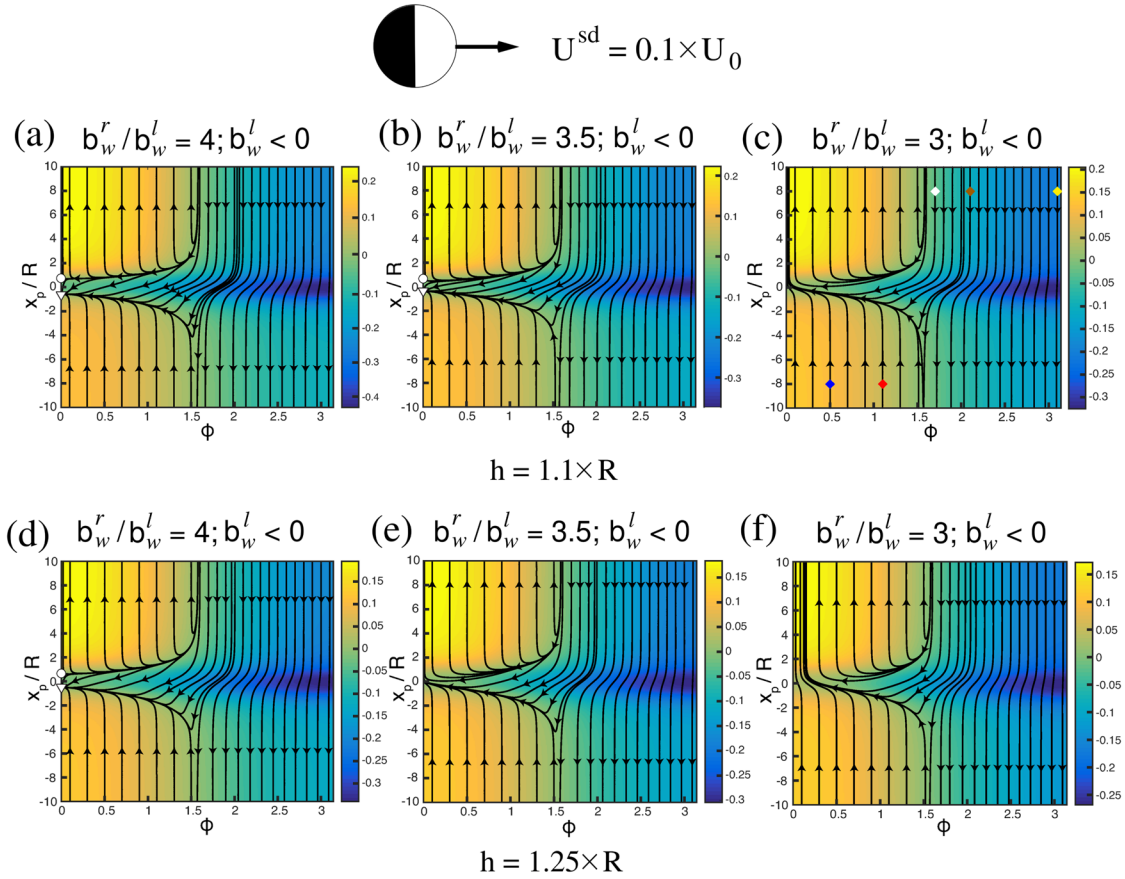

FIG. 3. Inert-forward Janus colloid with $\mathbf{U}^{sd} \cdot \hat{\mathbf{d}} = 0.1 \times U_0$ at a chemical step, where $\mathbf{U}^{sd}$ is the self-diffusiophoretic component of the particle velocity and $\hat{\mathbf{d}}$ is the direction of the self-diffusiophoretic motion. Effects of the wall chemical contrast on the topology of the phase portrait in the (ϕ, x_p) plane. The wall contrast is varied by varying $\zeta = b_w^r/b_w^l > 0$ at constant negative b_w^l. Here, b_w^r and b_w^l are the surface mobility coefficients for the right and the left part of the wall, respectively. The top row corresponds to $h = 1.1 \times R$ with (a) $\zeta = 4$, (b) $\zeta = 3.5$, and (c) $\zeta = 3$. The bottom row has $h = 1.25 \times R$ with (d) $\zeta = 4$, (e) $\zeta = 3.5$, and (f) $\zeta = 3$. The white triangles in (a), (b), and (d) at $\phi = 0°$ and for x_p slightly below zero depict the stable fixed points which we call "docking" states. The white circles in (a), (b), and (d) at $\phi = 0°$ and for x_p slightly above zero depict the saddle fixed points. The five diamond symbols in (c) give the initial conditions corresponding to the trajectories shown in Fig. 6. The background color encodes U_x/U_0, where $U_0 \equiv 2|b_w^l|\alpha_0/D$.

being an input parameter. The docking condition $U_x^{tot} = 0$ yields the following estimate for the threshold value U_c^{sd}:

$$-U_c^{sd}\cos(\phi) = \frac{3\alpha_0 R^2(b_w^r - b_w^l)}{16Dh^2} - \frac{|\alpha_1|R^3(b_w^r + b_w^l)}{32Dh^3}\cos(\phi). \quad (17)$$

If $b_w^l > b_w^r$, one has $\phi = 0°$ for the docking configuration (see Fig. 3), whereas for $b_w^l < b_w^r$, one has $\phi = 180°$ at the docking configuration. Accordingly, we obtain

$$U_c^{sd} = \frac{3\alpha_0 R^2|b_w^l - b_w^r|}{16Dh^2} + \frac{|\alpha_1|R^3(b_w^r + b_w^l)}{32Dh^3}, \quad (18)$$

which renders a line in the (U^{sd}, h) plane, separating docking and crossing particle states (see Fig. 5).

It is instructive to take a closer look at the structure of the phase portraits and at the shape of some representative particle trajectories in the (ϕ, x_p) plane. For sufficiently strong chemical contrast ζ, as in Figs. 3(a), 3(b), and 3(d), all trajectories can be classified into three groups. The first group contains the trajectories leading to the docking fixed point, marked by white triangles in Figs. 3(a), 3(b), and 3(d). All particles approaching the step from the left and with orientation $\phi < \pi/2$ will dock. The first group also contains a bundle of trajectories with $\pi/2 < \phi \lesssim 2$ and which approach the step from the right. In the second group, which includes all trajectories with $\phi \gtrsim 2$, trajectories cross over the step from the right. Finally, the third group consists of trajectories according to which the particle is initially located on the right side of the step and is oriented away from the step, as in the upper left corner of Figs. 3(a), 3(b), and 3(d). In this case, the particle simply moves directly away from the step and escapes.

Decreasing the chemical contrast ζ, the docking state and the saddle point approach each other in the (x_p, ϕ) plane, and eventually collide and annihilate. For ζ below the annihilation value, as in

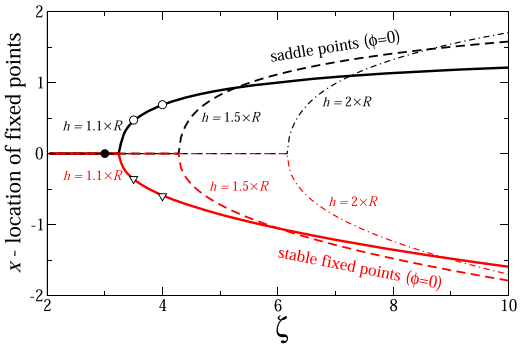

FIG. 4. The dependence of the x-location of fixed points on the chemical contrast $\zeta \equiv b^r_w/b^l_w$ for an inert-forward Janus colloid with $U^{sd} = \mathbf{U}^{sd}\cdot\hat{\mathbf{d}} = 0.1\times U_0$ and for several values of the distance h from the wall. Here, $\mathbf{U}^{sd}$ is the self-diffusiophoretic component of the particle velocity and $\hat{\mathbf{d}}$ is the direction of the self-diffusiophoretic motion. The surface mobility coefficient of the left side of the substrate b^l_w is kept constant and negative: $U_0 \equiv 2|b^l_w|\alpha_0/D$. The open triangles and open circles on the curve $h = 1.1 \times R$ correspond to the systems shown in Figs. 3(a) and 3(b), while the black solid circle corresponds to the system in Fig. 3(c).

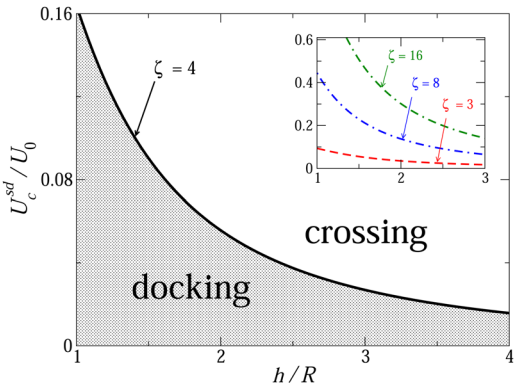

FIG. 5. Upper critical self-diffusiophoretic velocity U_c^{sd}, for which a particle can dock at the step, as a function of h/R. The curves are obtained from Eq. (18): $U_0 \equiv 2|b^l_w|\alpha_0/D$ and $\zeta = b^r_w/b^l_w$.

Figs. 3(c), 3(e), and 3(f), the phase portraits reveal four groups of trajectories: reflected trajectories, trajectories which cross from the right, direct escape trajectories, and trajectories which cross from the left. Reflection occurs for particles approaching the step from the right and with orientations in a narrow band $\pi/2 \le \phi \lesssim 2$. One example of a reflecting trajectory is shown in Fig. 6(a); the corresponding initial position and orientation are marked by the white diamond in Fig. 3(c). For this particular initial condition, the particle penetrates slightly into the orange (less repulsive) region of the substrate before turning around and moving back into the gray region. By increasing the initial orientation ϕ as compared to that of the white diamond, we may increase the extent of the penetration into the orange side, up to a maximum of two particle diameters. With a

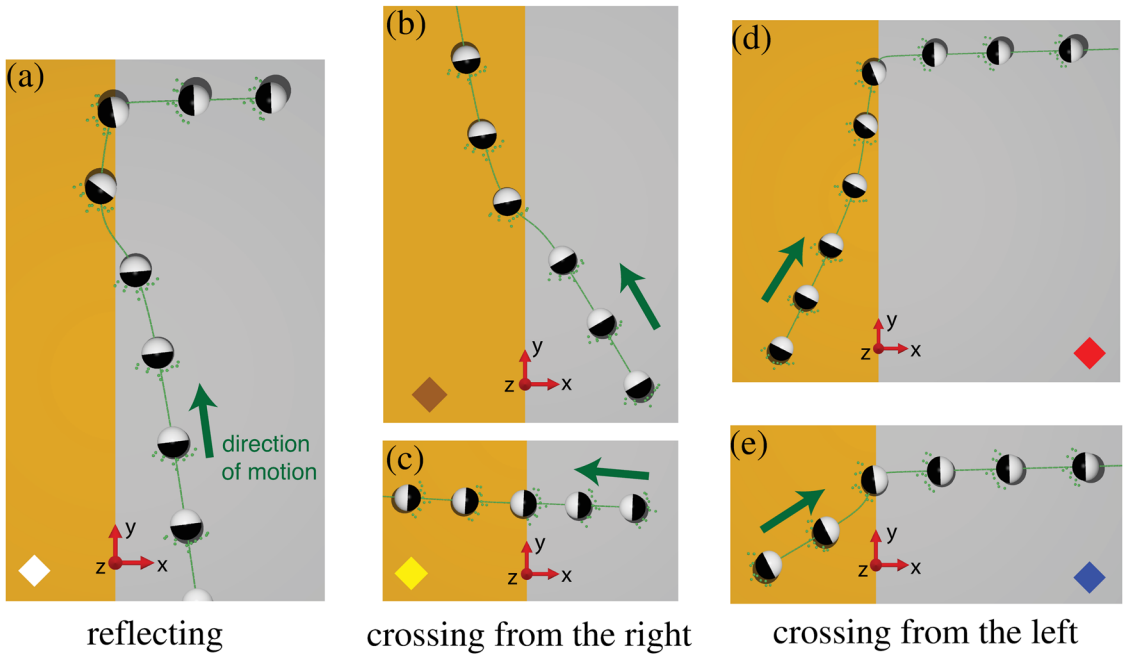

FIG. 6. Representative trajectories of an inert-forward ($\mathbf{U}^{sd}\cdot\hat{\mathbf{d}} = 0.1\times U_0$, $U_0 \equiv 2|b^l_w|\alpha_0/D$) particle near a chemical step with contrast $b^r_w/b^l_w = 3$, $b^l_w < 0$. The diamond symbols match with the initial position $x_p = x_p^0$ and orientation $\phi = \phi^0$ of the trajectories in Fig. 3(c): (a) $x_p^0 = 10\times R$, $\phi^0 \simeq 1.7$; (b) $x_p^0 = 10\times R$, $\phi^0 \simeq 2.2$; (c) $x_p^0 = 10\times R$, $\phi^0 \simeq 3.1$; (d) $x_p^0 = -10\times R$, $\phi^0 \simeq 1.1$; and (e) $x_p^0 = -10\times R$, $\phi^0 \simeq 0.5$. The trajectories are shown to scale with the colloid size, i.e., the penetration depth in (a) is indeed given in units of the particle radius.

further increase in the orientation, we find the group of trajectories which cross from the right to the left. This group includes the initial conditions indicated by the brown and yellow diamonds in Fig. 3(c), which correspond to the trajectories shown in Figs. 6(b) and 6(c), respectively. The exit orientations ϕ of these trajectories are slightly smaller than the initial orientations. If, starting from the white diamond, we decrease the initial orientation, we encounter the group of directly escaping trajectories [upper left corner of Figs. 3(c), 3(e), and 3(f)]. Finally, for trajectories which start in the lower left corner of Figs. 3(c), 3(e), and 3(f), the particle crosses over the step with exit orientation $\phi \ll 1$. In other words, the step operates as a trajectory focusing device for particles which cross from the left. This group includes the initial conditions indicated by the blue and red diamonds in Fig. 3(c), corresponding to the trajectories shown in Figs. 6(d) and 6(e).

B. Phase portraits in the (ϕ, x_P) plane for catalyst-forward colloids

Figure 7 shows how the topology of the phase portraits for catalyst-forward ($U^{sd} = \mathbf{U}^{sd} \cdot \hat{\mathbf{d}} < 0$) particles varies with the chemical contrast $\zeta = b_w^r/b_w^l$. This system has no stable fixed point. The physical reason for this is that now both the monopole and the self-diffusiophoretic components drive the particle away from the step into the orange, less repulsive region of the surface. The dipole contribution to the angular velocity still rotates the particle into the configuration $\phi = 0$. We find only saddle points, marked by white circles in Figs. 7(a), 7(b), and 7(d), and unstable fixed points, marked by black circles in Figs. 7(c) and 7(d). The dependence of the spatial locations of the saddle points x_p° and of the unstable fixed points $x_p^\bullet$ on the chemical contrast ζ is presented in Fig. 8.

The location of the saddle point within the orange area ($x_p^\circ < 0$) with $\phi = \pi$ (the catalytic cap facing the gray, more repulsive side of the substrate) depends only weakly on ζ within the studied range (see the blue curve in Fig. 8). The location x_p° is determined by the balance between the chemiosmotic contribution, which drives the particle away from the step, and the self-diffusiophoretic velocity, which is directed toward the step. The orientation $\phi = \pi$ is not stable with respect to Ω_z^{dp} which favors $\phi = 0$. At small enough $\zeta = \zeta^{bif}$ (from *bif*urcation), this point collides with the upper ($x_p^\bullet > 0$) unstable fixed point, and both disappear upon further decrease in ζ.

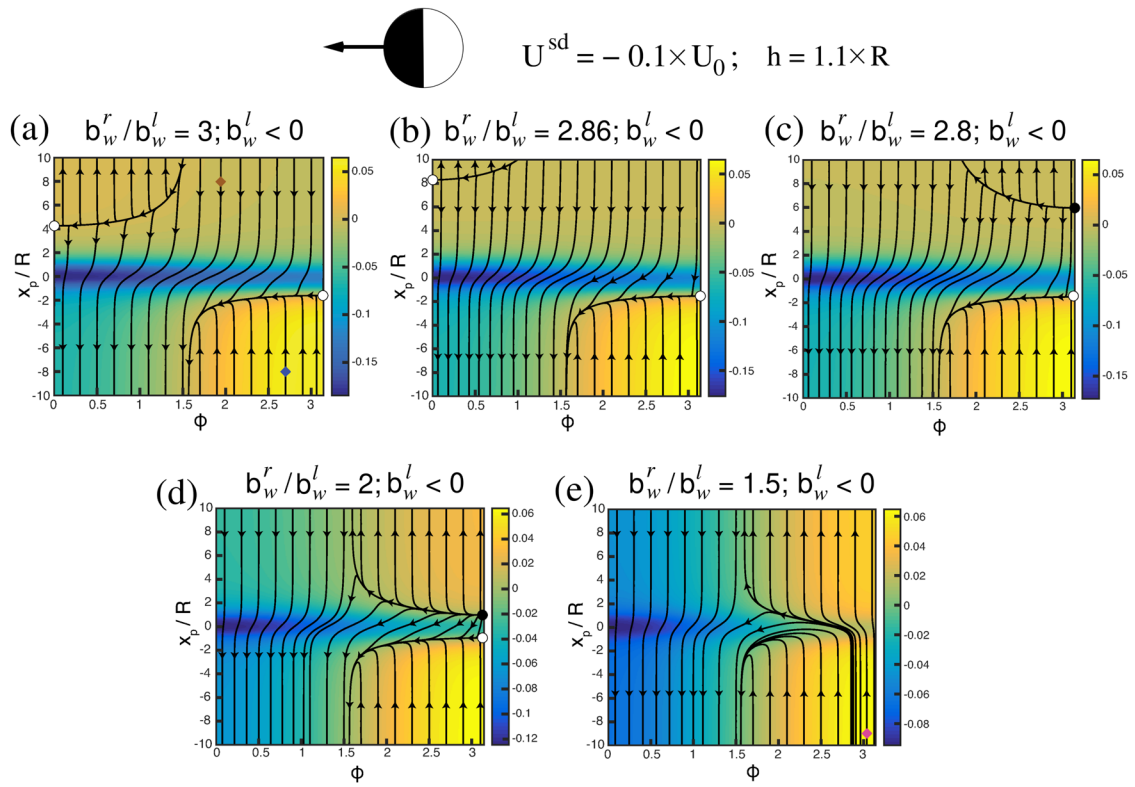

FIG. 7. Catalyst-forward Janus colloid with $\mathbf{U}^{sd} \cdot \hat{\mathbf{d}} = -0.1 \times U_0$ at a chemical step, where $\mathbf{U}^{sd}$ is the self-diffusiophoretic component of the particle velocity and $\hat{\mathbf{d}}$ is the direction of the self-diffusiophoretic motion. Influence of the wall chemical contrast $\zeta = b_w^r/b_w^l > 0$, with $b_w^l < 0$, on the topology of the phase portrait in the (ϕ, x_p) plane at $h = 1.1 \times R$ and at (a) $\zeta = 3$, (b) $\zeta = 2.86$, (c) $\zeta = 2.8$, (d) $\zeta = 2$, and (e) $\zeta = 1.5$. Here, b_w^r and b_w^l are the surface mobility coefficients for the right and the left part of the wall, respectively, and h is the particle-wall distance. The white circles in (a)–(d) depict the saddle fixed points; the black circles in (c) and (d) denote the unstable fixed points. The brown and blue diamonds in (a) and the pink diamond in (e) indicate the initial conditions corresponding to the trajectories in Fig. 9. The background color encodes U_x/U_0 with $U_0 \equiv 2|b_w^l|\alpha_0/D$.

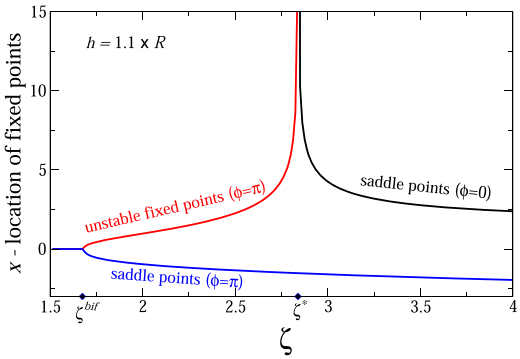

FIG. 8. The dependence of the x-location of various fixed points on the chemical contrast $\zeta \equiv b_w^r/b_w^l$, $b_w^l < 0$, for a catalyst-forward Janus colloid with $\mathbf{U}^{sd} \cdot \hat{\mathbf{d}} = -0.1 \times U_0$, and $h = 1.1 \times R$; $U_0 \equiv 2|b_w^l|\alpha_0/D$; here, $\mathbf{U}^{sd}$ is the self-diffusiophoretic component of the particle velocity, $\hat{\mathbf{d}}$ is the direction of the self-diffusiophoretic motion, and h is the particle-wall distance. Bifurcation occurs at $\zeta^{bif} \simeq 1.675$. The black curve diverges at $\zeta^* \simeq 2.839$.

The location of the second saddle point located within the gray area ($x_p^\circ > 0$) with $\phi = 0$ diverges if ζ approaches a certain critical value ζ^* from above (see the black curve in Fig. 8). This again may be understood by balancing the chemiosmotic and self-diffusiophoretic components to the velocity in the x-direction. For $x_p \gg 1$, the chemiosmotic contribution $U_x^{ws} \simeq U_x^{mp} + U_x^{dp}$ behaves as

$$U_x^{ws}(x_p \gg 1) \sim |b_w^l|\left[\frac{|\alpha_1|R^3\zeta\cos(\phi)}{16Dh^3} - (\zeta-1)\frac{3\alpha_0 R^2 h}{8Dx_p^3}\right] > 0, \quad (19)$$

i.e., at large x_p, it "pushes" the particle away from the step. The self-diffusiophoretic component points in the opposite direction. Both terms on the rhs of Eq. (19) are positive, and the second term is a correction $\mathcal{O}(1/x_p^3)$ to the first one. Since for ζ near the critical value ζ^* the magnitude of U_x^{ws} in Eq. (19) decreases with decreasing ζ and increases with increasing x_p, the balance of the two velocity components occurs at increasingly larger distances from the step as $\zeta \searrow \zeta^*$. At $\zeta = \zeta^*$, the chemical contrast is too weak, and the induced chemiosmotic component cannot balance the self-diffusiophoretic speed. Similar arguments explain the divergence of the location of the unstable fixed point $x_p^\bullet > 0$ at $\phi = \pi$ as ζ approaches ζ^* from below. In this case, $U_x^{ws} < 0$ at large x_p [Fig. 2(b)], i.e., the chemiosmotic contribution pushes the particle toward the step, while the self-diffusiophoretic velocity is directed away from the step. The divergences are described by the following asymptotic forms (valid for $x_p \to \infty$):

$$x_p^\circ(\zeta \searrow \zeta^*, \phi = 0) = R\left[\frac{6\alpha_0(\zeta-1)(h/R)^4}{|\alpha_1|}\right]^{\frac{1}{3}}(\zeta-\zeta^*)^{-\frac{1}{3}}, \quad \text{saddle},$$
$$x_p^\bullet(\zeta \nearrow \zeta^*, \phi = \pi) = R\left[\frac{6\alpha_0(\zeta-1)(h/R)^4}{|\alpha_1|}\right]^{\frac{1}{3}}(\zeta^*-\zeta)^{-\frac{1}{3}}, \quad \text{unstable}, \quad (20)$$

where $\zeta^* \equiv -32(\alpha_0/|\alpha_1|)(h/R)^3 U^{sd}/U_0$. These formulae have been obtained as follows: First, we carry out the Taylor expansion of the rhs of Eq. (4) in terms of powers of $1/x_p$, retaining only the leading $[\mathcal{O}(1)]$ and next-to-leading $[\mathcal{O}(1/x_p^3)]$ terms. Next, we equate the truncated series to zero and solve the resulting equation with respect to x_p. This provides the desired asymptotic behavior.

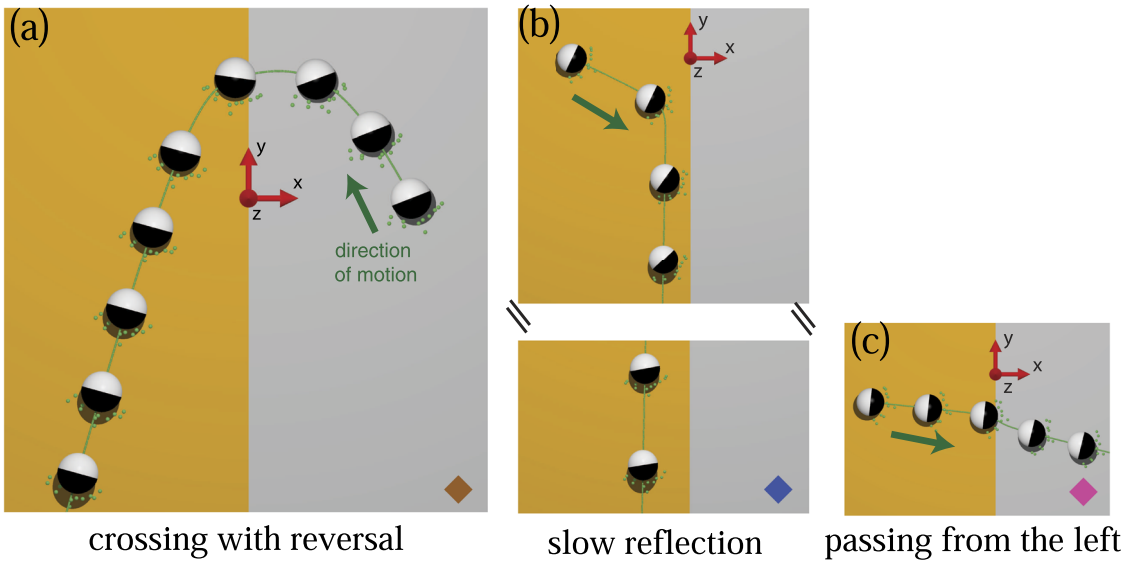

FIG. 9. Representative trajectories of a catalyst-forward ($\mathbf{U}^{sd} \cdot \hat{\mathbf{d}} = -0.1 \times U_0$, where $U_0 \equiv 2|b_w^l|\alpha_0/D$) particle near a chemical step. The diamond symbols match with the initial position $x_p = x_p^0$ and orientation $\phi = \phi^0$ of the trajectories in Figs. 7(a) and 7(e): (a) $x_p^0 = 10 \times R$, $\phi^0 \simeq 1.9$; (b) $x_p^0 = -10 \times R$, $\phi^0 \simeq 2.7$; and (c) $x_p^0 = -10 \times R$, $\phi^0 \simeq 3.05$.

For $\zeta > \zeta^*$, the phase plane is split into three regions: the escaping region, located in the upper left corner in Figs. 7(a) and 7(b); the crossing region, extending across all ϕ at $x_p = 0$; and the reflecting region, located in the bottom right corner of Figs. 7(a) and 7(b). A typical crossing trajectory is shown in Fig. 9(a). The initial position and orientation of the particle is indicated by the brown diamond in Fig. 7(a). The particle approaches the step from the right, having its inert part at the front. This is due to the chemiosmotic contribution U_x^{ws}, which is strong enough to overcome the intrinsic (i.e., self-diffusiophoretic) tendency of the particle to move catalyst-forward. At the step, the direction of motion reverses and the particle moves away from the step with the cap in the front. In Fig. 9(b), we present a typical reflecting trajectory, with the initial conditions indicated by the blue diamond in Fig. 7(a). The particle approaches the step from the left; this initial part of the trajectory is fast. Next, the particle slowly reorients its direction and leaves the step with an asymptotic exit angle $\phi = \pi/2$.

For $\zeta^{bif} < \zeta < \zeta^*$, the escaping region changes its location; it is now in the upper right hand corner in Figs. 7(c) and 7(d). The crossing and reflecting regions are present as well. Finally, for $\zeta < \zeta^{bi,f}$, there are no fixed points; the phase plane has only crossing and reflecting regions. However, now the crossing may proceed either from the right or from the left; see Fig. 9(c) for which the initial condition corresponds to the pink diamond in Fig. 7(e). For the trajectories which cross from the left ($x_p < 0$), a small bundle of initial angles ϕ is spread over a much broader range of exit angles, i.e., the chemical step operates as an "angular dispersion" device.

V. CHEMICAL STRIPES

We now consider a substrate with a chemical stripe of width $2W$. We take $b(\mathbf{x}_s) = b_w^l$ for $x < -W$, $b(\mathbf{x}_s) = b_w^c$ for $-W < x < W$, and $b(\mathbf{x}_s) = b_w^r$ for $x > W$. We discuss the special case $b_w^r = b_w^l \equiv b_w$. However, for reasons of generality, in the following equations, we allow the sides to the left and to the right of the stripe to differ. Accordingly, the integral in Eq. (A4) consists of three pieces,

$$V_j = b_w^l \int_{-\infty}^{-W} dx \int_{-\infty}^{\infty} dy \left(\nabla_{||} c \cdot \boldsymbol{\sigma}'^{(j)} \cdot \hat{\mathbf{z}}\right) + b_w^c \int_{-W}^{W} dx \int_{-\infty}^{\infty} dy \left(\nabla_{||} c \cdot \boldsymbol{\sigma}'^{(j)} \cdot \hat{\mathbf{z}}\right) + b_w^r \int_{W}^{\infty} dx \int_{-\infty}^{\infty} dy \left(\nabla_{||} c \cdot \boldsymbol{\sigma}'^{(j)} \cdot \hat{\mathbf{z}}\right). \quad (21)$$

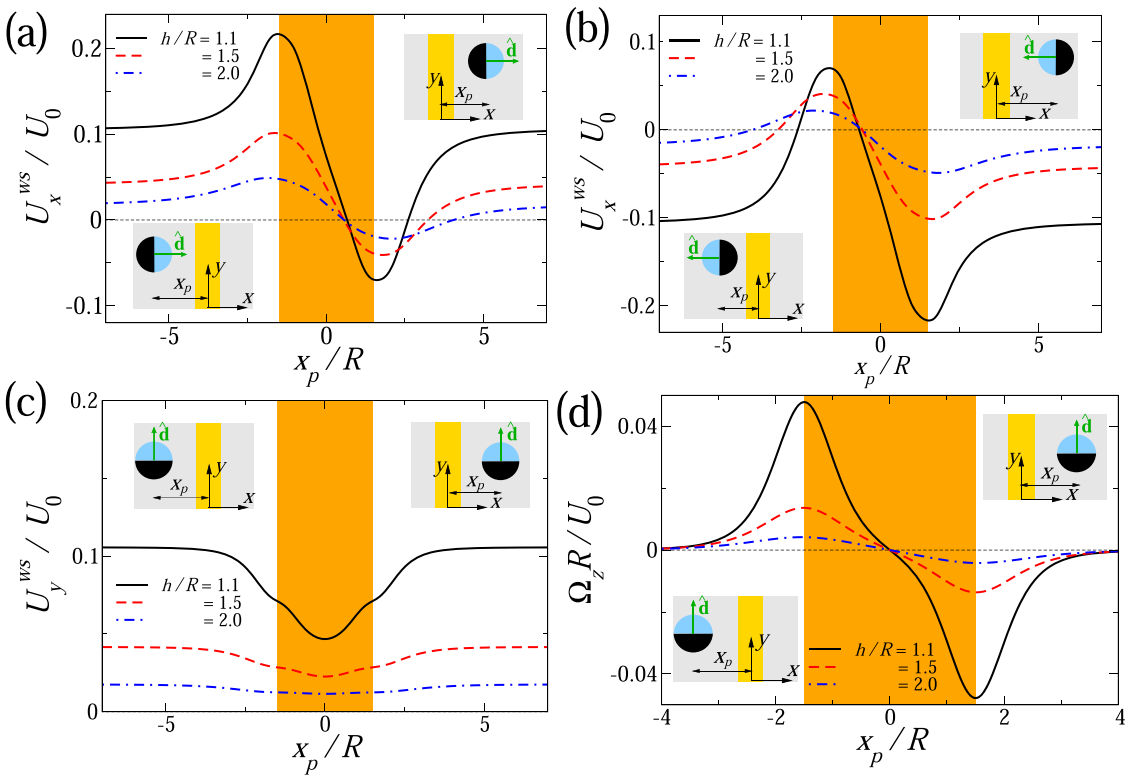

FIG. 10. A Janus particle at a chemical stripe with $2W/R = 3$, $b_w^l = b_w^r$, $b_w^l/b_w^c = 3$, and $b_w^c < 0$. [(a) and (b)] Chemiosmotic contribution $U_x^{ws} \simeq U_x^{mp} + U_x^{dp}$ [see Eqs. (22) and (23)] to the particle translational velocity as a function of x_p for a particle with orientation $\phi = 0°$ and $\phi = 180°$, respectively. (c) Chemiosmotic contribution $U_y^{ws} \simeq U_y^{dp}$ [see Eq. (24)] to the particle translational velocity as a function of x_p for a particle oriented parallel ($\phi = 90°$) to the stripe. (d) Angular velocity, calculated from Eq. (25), of a particle oriented parallel ($\phi = 90°$) to the stripe as a function of x_p: $U_0 \equiv 2|b_w^c|\alpha_0/D$.

Along the lines of Subsection IV, we obtain

$$U_x^{mp} = \frac{3hR^2\alpha_0}{16D}\left[\frac{(b_w^c - b_w^l)(h^2+2(x_p+W)^2)}{(h^2+(x_p+W)^2)^{5/2}} + \frac{(b_w^r - b_w^c)(h^2+2(x_p-W)^2)}{(h^2+(x_p-W)^2)^{5/2}}\right], \tag{22}$$

$$U_x^{dp} = -\frac{|\alpha_1|R^3}{256Dh^3}\left[-8(b_w^r+b_w^l)+(b_w^c-b_w^r)\times\frac{(-25\,h^4+28h^2(x_p-W)^2+8(x_p-W)^4)(x_p-W)^3}{(h^2+(x_p-W)^2)^{7/2}} + (b_w^l-b_w^c)\frac{(-25\,h^4+28h^2(x_p+W)^2+8(x_p+W)^4)(x_p+W)^3}{(h^2+(x_p+W)^2)^{7/2}}\right]\times\cos(\phi), \tag{23}$$

$$U_y^{dp} = \frac{|\alpha_1|R^3}{256Dh^3}\left[-8(b_w^r+b_w^l)+(b_w^c-b_w^r)\times\frac{(8(x_p-W)^4+20h^2(x_p-W)^2+3h^4)(x_p-W)}{(h^2+(x_p-W)^2)^{5/2}} + (b_w^l-b_w^c)\frac{(8(x_p+W)^4+20h^2(x_p+W)^2+3h^4)(x_p+W)}{(h^2+(x_p+W)^2)^{5/2}}\right]\times\sin(\phi), \tag{24}$$

and

$$\Omega_z^{dp} = -\frac{3hR^3|\alpha_1|}{64D}\left[\frac{(b_w^c-b_w^r)}{(h^2+(x_p-W)^2)^{5/2}} + \frac{(b_w^l-b_w^c)}{(h^2+(x_p+W)^2)^{5/2}}\right]\sin(\phi). \tag{25}$$

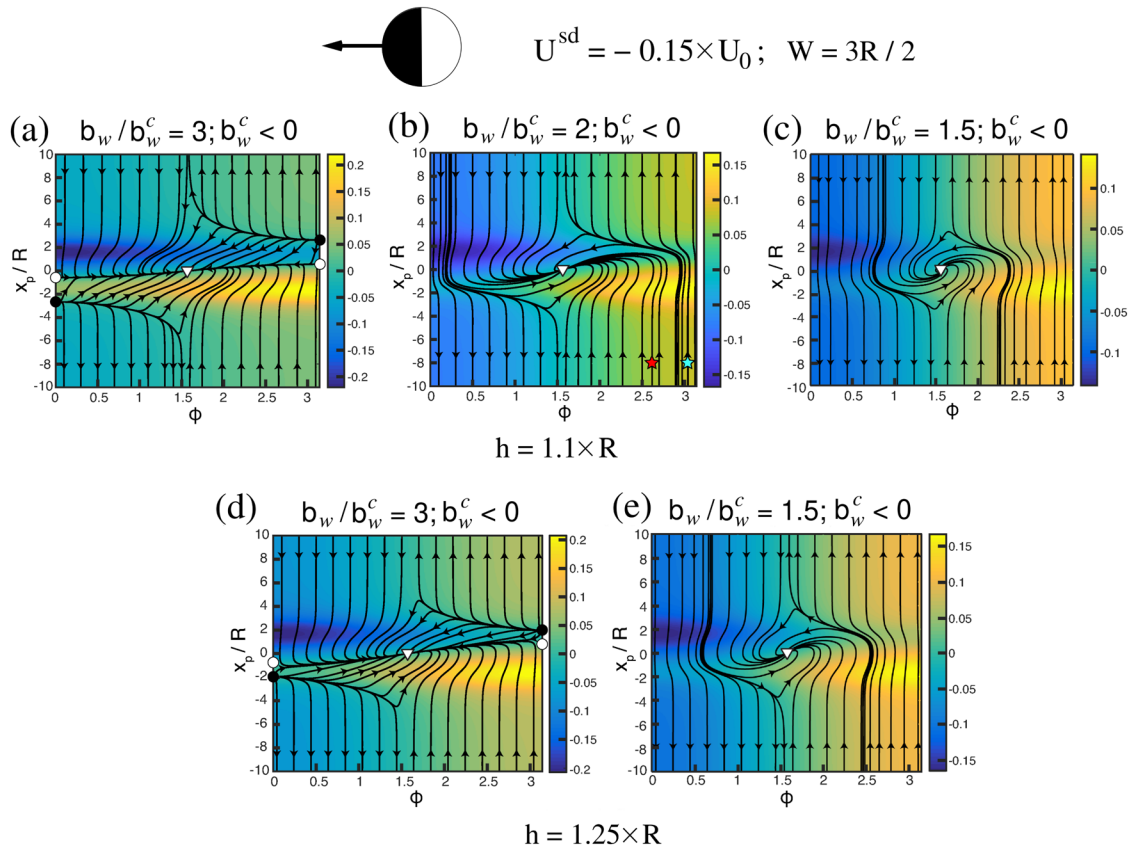

FIG. 11. Catalyst-forward Janus particle near a chemical stripe of width $W = 1.5 \times R$. The figure shows the effect of the wall chemical contrast on the topology of the phase portrait in the (ϕ, x_p) plane with $\mathbf{U}^{sd} \cdot \hat{\mathbf{d}} = -0.15 \times U_0$, where $U_0 \equiv 2|b_w^c|\alpha_0/D$. The wall contrast is varied by varying $b_w^l = b_w^r \equiv b_w$ with $b_w^c < 0$. The results obtained for two different values of the particle-wall separation h are presented. The first row corresponds to $h = 1.1 \times R$ at (a) $b_w/b_w^c = 3$, (b) $b_w/b_w^c = 2$, and (c) $b_w/b_w^c = 1.5$. The second row corresponds to $h = 1.25 \times R$ at (d) $b_w/b_w^c = 3$ and (e) $b_w/b_w^c = 1.5$. There is an attractor marked by the white triangle at $x_p = 0$ and $\phi = \pm\pi/2$ (we recall the mirror symmetry with respect to $\phi = \pi$). Additionally, in (a) and (d), there are saddle points (white circles) and unstable fixed points (black circles). The background color encodes U_x/U_0. The star symbols in (b) indicate the initial conditions for the trajectories shown in Fig. 12.

We note that, as in the case of a chemical step, there is no dependence on y_p due to the translational invariance of the system along the y-direction.

In Fig. 10, we show the chemiosmotic contributions $U_x^{ws} \simeq U_x^{mp} + U_x^{dp}$ [Eqs. (22) and (23)], $U_y^{ws} \simeq U_y^{dp}$ [Eq. (24)], and Ω_z^{dp} [Eq. (25)] as a function of x_p and for various orientations ϕ. The velocities are presented in units of $U_0 \equiv 2|b_w^c|\alpha_0/D$. (In this section, for reasons of simplicity, we use the same notation U_0 for the velocity scale as in Secs. IV A and IV B.) When a particle is oriented perpendicular to the stripe [$\phi = 0$ in Fig. 10(a)], U_x^{ws} drives the particle from the regions $x_p < 0$ and $0 < x_p \lesssim 2.5 \times R$ to the center of the stripe, where the angular velocity Ω_z^{dp} reorients the axis of the particle to $\phi = \pi/2$, i.e., parallel to the edges of the stripe. In this configuration [$(\phi, x_p) = (\pi/2, 0)$], only $U_y^{dp} \neq 0$. We find that for a catalyst-forward particle ($\mathbf{U}^{sd} \cdot \hat{\mathbf{d}} < 0$), this mechanism leads to a stable motion along the stripe. In order to understand the stability of the configurations with $\phi = \pm\pi/2$, we consider a small perturbation $\delta\phi$. The particle starts moving toward one of the stripe edges because for $\phi \neq \pi/2$ one has $U_x^{sd} \neq 0$. At the same time, the edge causes rotation of the cap toward the center of the stripe,[51] dampening $\delta\phi$ for a catalyst-forward particle. In contrast, for an inert-forward ($\mathbf{U}^{sd} \cdot \hat{\mathbf{d}} > 0$) particle, the edge driven rotation of the cap enhances $\delta\phi$ and may lead to the docking of the particle at the edge, provided its self-diffusiophoretic velocity component is not too large. More details concerning the stability of the stripe-following trajectories may be found in Ref. 51. Intriguingly, the dynamical mechanism by which a catalyst-forward particle can follow a chemical stripe resembles the mechanism by which a magnetic bacterium can follow a magnetic stripe domain on a garnet substrate.[56] However, the physical origin of stripe-following dynamics is different in the two cases.

Next, we explore how the chemical contrast between the stripe and the rest of the surface influences the topology of the phase plane. Figure 11 summarizes the results for a catalyst-forward particle, which reveals a stable attractor at $x_p = 0$ and $\phi = \pm\pi/2$ (white triangles), corresponding to the particle moving along the stripe in the upward or downward direction. Additionally, we find saddle points (white circles) and unstable fixed points (solid black circles) at $\phi = 0$ and $\phi = \pi$ for sufficiently strong chemical contrast b_w/b_w^c [see Figs. 11(a) and 11(d)]. In this case, the phase plane is dominated by the stable attractor as it features the largest basin of attraction. The two unstable fixed points control the escaping regions of the phase plane in the lower left and upper right corners of Figs. 11(a) and 11(d). Similar to the case of the chemical step, the locations of the saddle points (white circles) at $\phi = 0$ and $\phi = \pi$ are determined by the balance between the chemiosmotic (driving the particles toward the stripe) and the self-diffusiophoretic (driving the particle away from the stripe) contributions to the particle velocity. Both orientations $\phi = 0$ and $\phi = \pi$ are unstable with respect to the stripe-driven rotation Ω_z^{dp} which favors $\phi = \pi/2$. For sufficiently small b_w/b_w^c, the chemiosmotic contribution is unable to balance the self-diffusiophoretic velocity and the saddle and unstable fixed points are not present [Figs. 11(b), 11(c),

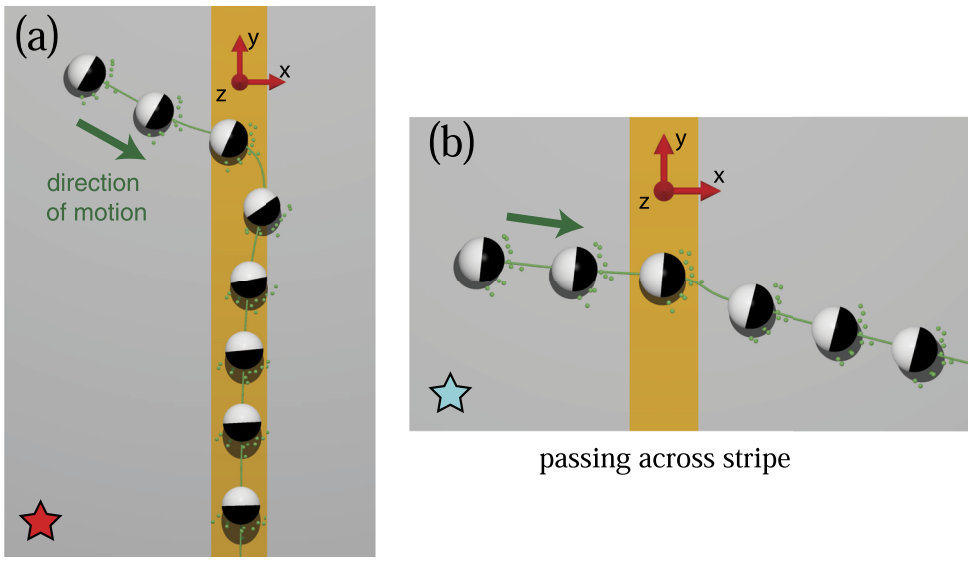

FIG. 12. Representative trajectories of an catalyst-forward ($\mathbf{U}^{sd} \cdot \hat{\mathbf{d}} = -0.15 \times U_0$, where $U_0 \equiv 2|b_w^c|\alpha_0/D$) particle near a chemical stripe. The star symbols match with the trajectories stemming from the initial positions and orientations in Fig. 11(b). (a) For certain values of the model parameters, a catalyst-forward particle attains the stripe-following steady state, which corresponds to the stable fixed point in the (ϕ, x_p) plane, depicted by white triangles in Fig. 11. For a moderate to a strong chemical contrast $b_w/b_w^c \gtrsim 2$, this attractor dominates the particle dynamics because it features the largest basin of attraction in the (ϕ, x_p) plane [see Figs. 11(a), 11(b), and 11(d)]. (b) Passing across the stripe occurs only for moderate values of b_w/b_w^c [see Figs. 11(b), 11(c), and 11(e)].

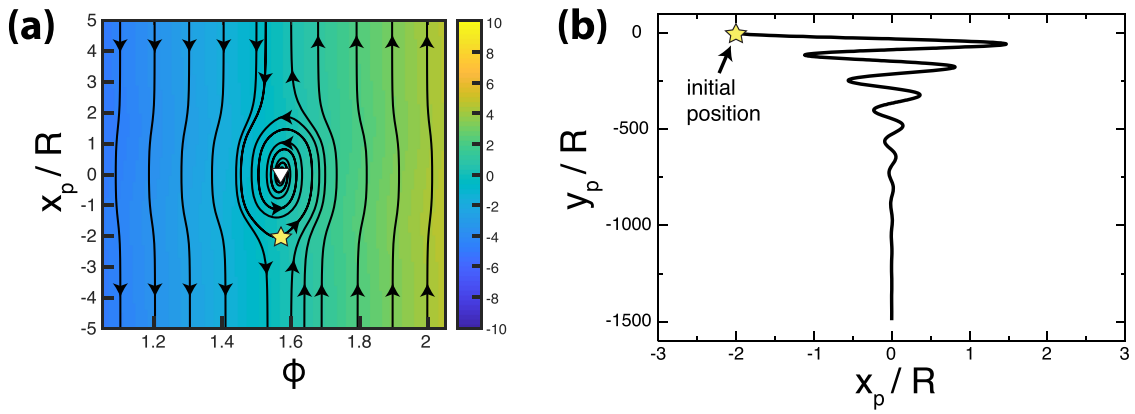

FIG. 13. (a) Phase plane for a very fast catalyst-forward particle ($\mathbf{U}^{sd} \cdot \hat{\mathbf{d}} = -10 \times U_0$, $h/R = 1.1$) near a stripe, with the same parameters as in Fig. 11(a): $2W/R = 3$, $b_w^l = b_w^r \equiv b_w = 3b_w^c$, and $b_w^c < 0$, with $U_0 \equiv 2|b_w^c|\alpha_0/D$. Remarkably, there is still an attractor (white triangle) at $x_p = 0$ and $\phi = \pi/2$, but the size of the basin of attraction is considerably reduced. (b) Trajectory for the same fast particle and the same stripe as in (a), with initial conditions $x_p/R = -2$, $y_p = 0$, and $\phi = \pi/2$, corresponding to the yellow star in (a). The particle position exhibits decaying oscillations about the center of the stripe.

and 11(e)]. In this case, in addition to the stripe-following trajectories [Fig. 12(a)], we find trajectories crossing the stripe from the right and from the left [see Fig. 12(b) for a trajectory crossing from the left].

Remarkably, the stripe-following state is stable even for very fast catalyst-forward particles, as shown in Fig. 13. Figure 13(a) shows a section of the phase plane for a particle with $U^{sd}/U_0 = -10$ and $h/R = 1.1$ near the stripe discussed in Fig. 11(a). There is still an attractor, although its basin is significantly reduced along the ϕ-axis. Interestingly, the particle configuration (x_p, ϕ) approaches the attractor via decaying oscillations. Figure 13(b) shows a real-space trajectory in the xy plane with the initial conditions $x_p/R = -2$, $y_p = 0$, and $\phi = \pi/2$. The trajectory exhibits decaying oscillations around the stripe center $x_p = 0$. The decay length of these oscillations is large in terms of the distance traveled by the particle in the y-direction; within a rough estimate, the particle is captured by the center when $y_p/R = -500$. The survival of the stripe-following attractor for very large $|U^{sd}|/U_0$ suggests that substrate materials with small phoretic mobility parameters, i.e., they either interact only very weakly or have a very short range of interaction with the solute, can still, if arranged into a stripe pattern, guide the motion of catalyst-forward particles.

VI. SUMMARY

We have studied the motion of catalytically active Janus spheres near a chemically patterned planar surface using the theoretical approach developed in Refs. 51 and 52. In particular, we have explored in detail the topology of the phase portraits as a function of the parameters characterizing the chemical contrast of the wall patterning. We have focused on the specific case of a particle with half of its surface covered by the catalyst. The particle-surface separation was taken to be constant, and the polar axis $\hat{\mathbf{d}}$ of the particle has been restricted to be parallel to the surface. The chemical activity of the particle drives chemiosmotic flows at the wall surface, which, in turn, induces flows in the volume of the solution. Consequently, the particle is advected by the surface-induced bulk flows. This chemiosmotic contribution to particle motion is sensitive to the chemical properties of the surface, and it may compete or cooperate with the intrinsic self-propulsion of the particle.

For the case of a single chemical step, we have considered both inert-forward and catalyst forward particles and we have investigated the effects of the surface chemical contrast and particle-surface separation on the particle dynamics. An inert-forward particle can cross the step, can be reflected from the step, or can stably dock at the contact line between the two surface regions, depending on the ratio $\zeta = b_w^r/b_w^l > 0$ of the surface phoretic mobilities, on the particle-wall distance h, and on the initial position and orientation of the particle. A docked particle has its polar axis aligned perpendicular to the interface. We have derived an approximate expression for the maximal self-phoretic velocity separating docking and crossing (Fig. 5). A particle which crosses the step can exhibit significant deviations of its orientation from the initial angle of approach [Figs. 3(c), 3(e), and 3(f)]. For example, all trajectories crossing the step from the left ($x_p < 0$), where the solute-wall repulsion is weaker than on the right side, have exit angles $\phi \ll 1$ [see the blue and red diamonds in Fig. 3(c)]. In other words, the chemical step operates as a trajectory focusing device. For steps with low chemical contrast, a particle can be reflected from the step when it approaches from the right ($x_p > 0$, where the solute-wall repulsion is stronger) and with an initial angle in a narrow band $\phi \gtrsim 90°$. The exit angle of the particle is again focused to $\phi \ll 1$ [see, e.g., the white diamond in Fig. 3(c), which corresponds to the trajectory in Fig. 6(a)].

Within the broad range of the parameters we have explored, the docking state has not been found for a catalyst-forward particle. Instead, however, depending on the initial conditions and the parameters of the system, the particle can cross the step, can be reflected by the step from the left, or can directly escape from the step. Crossing the step from the right to left is possible for any value of the chemical contrast ζ [see Fig. 7 and the particle real space

trajectory in Fig. 9(a)]. In this case, the difference between the initial and the exit angles of the particle is moderate. For sufficiently small ζ, a particle can cross the step from the left to right [see Fig. 7(e) and the particle real space trajectory in Fig. 9(c)], with the initial angle $\phi \lesssim 180^\circ$ and the exit angle in the range $90^\circ < \phi < 180^\circ$. For intermediate to high chemical contrasts ζ, as well as for a broad range of initial angles at low chemical contrast, a particle approaching from the left is reflected for all initial angles of approach $\phi > 90^\circ$ [see the lower right corners in Fig. 7, as well as the reflecting trajectory in Fig. 9(b)]. For intermediate values of the chemical contrast, a catalyst-forward particle can directly escape from the step if it starts from the right and slightly above the separatrix [see the upper right hand corners in Figs. 7(c) and 7(d)]. At high contrast, the region of escape is in the upper left corner of the phase portrait [Figs. 7(a) and 7(b)].

We have also considered a catalyst-forward particle at a surface which exhibits a narrow chemical stripe. We have found a stable stripe-following state in which the particle moves along the stripe center and is perfectly aligned with the stripe [Fig. 12(a)]. Surprisingly, the stripe-following state is present at all values of the chemical contrast larger than unity, although its basin of attraction may be small [Fig. 11(c)]. For sufficiently strong chemical contrast, a particle never crosses the stripe [Figs. 11(a) and 11(d)]; instead, the particle either stably follows the stripe or directly moves away from it, depending on the initial position and orientation. For smaller values of the chemical contrast, a particle can cross the stripe from either the left or the right [Figs. 11(b), 11(c), and 11(e)]. We have not found the stripe-following state for inert-forward particles.

Finally, our approach considers the particle to be restricted to a constant height h above the wall and its orientation $\hat{\mathbf{d}}$ to stay within the plane of the substrate. This assumption is supported by the observation that for two given surfaces with distinct chemistry, the parameters of a Janus particle may be adjusted such that it will have similar stable values h^* and $\hat{\mathbf{d}}^*$ at both surfaces. In other words, such a "designed" Janus particle will self-adjust to in-plane motion employing only internal phoretic mechanisms (such as self-diffusiophoresis or self-electrophoresis), combined with hydrodynamic and chemical interactions with the wall. Additionally, such wall-bounded two-dimensional motion may be achieved by using magnetic fields for particles containing a magnetic core.[8,57]

Intriguingly, the behavior of the self-phoretic particle bears certain similarities to the motion of a motile magnetic bacterium guided by static magnetic fields emanating from stripe domains in a garnet substrate.[56]

ACKNOWLEDGMENTS

W.E.U., M.T., and M.N.P. acknowledge financial support from the German Research Foundation (DFG) (Grant No. TA 959/1-1). M.T. acknowledges financial support from the Portuguese Foundation for Science and Technology (FCT) under Contract Nos. IF/00322/2015 and UID/FIS/00618/2019.

APPENDIX A: CALCULATION OF $\mathbf{U}^{ws}$ AND $\boldsymbol{\Omega}^{ws}$

In order to obtain $\mathbf{U}^{ws}$ and $\boldsymbol{\Omega}^{ws}$, we set $\mathbf{v}_s(\mathbf{x}_s) = 0$ at the particle surface [see Eq. (3) and below it] and use the Lorentz reciprocal theorem.[55] This theorem relates the fluid stresses $(\boldsymbol{\sigma}, \boldsymbol{\sigma}')$ and the velocity fields $(\mathbf{u}, \mathbf{u}')$ of two solutions to the Stokes equation within the same domain

$$\int \mathbf{u} \cdot \boldsymbol{\sigma}' \cdot \hat{\mathbf{n}}\, dS = \int \mathbf{u}' \cdot \boldsymbol{\sigma} \cdot \hat{\mathbf{n}}\, dS, \tag{A1}$$

where the surface integrals are taken over the fluid domain boundaries, and $\hat{\mathbf{n}}$ is the surface unit normal vector pointing into the fluid domain. We take the "unprimed" problem to be the one specified above for the six unknowns $\mathbf{V} \equiv (\mathbf{U}^{ws}, \boldsymbol{\Omega}^{ws})$, requiring six "primed" subproblems. We recall that for the unprimed problem, the boundary conditions are $\mathbf{u} = \mathbf{v}_s$ at the planar wall, $\mathbf{u} = \mathbf{U}^{ws} + \boldsymbol{\Omega}^{ws} \times (\mathbf{x} - \mathbf{x}_0)$ at the particle surface, and $\mathbf{u} = 0$ at infinity. Note that here $\mathbf{v}_s$ has already been determined from the solution of the Laplace equation; thus, it is a known quantity.

For the primed subproblems $(\mathbf{u}'^{(j)}, \boldsymbol{\sigma}'^{(j)})$, indexed by j, we consider an inactive particle subject to an external force of unit magnitude in the $\hat{x}$, $\hat{y}$, or $\hat{z}$ direction for $j = 1, 2, 3$, or an external, also unit magnitude torque in $\hat{x}$, $\hat{y}$, or $\hat{z}$ ($j = 4, 5, 6$). For each of the cases $j = 1, \ldots, 6$, we impose that the motion is subject to no-slip boundary conditions, i.e., $\mathbf{u}'^{(j)} = 0$ at the planar wall, and that the fluid is quiescent far away from the particle, i.e., $\mathbf{u}'^{(j)} = 0$ at infinity. At the particle surface, there is a no-slip condition which implies $\mathbf{u}'^{(j)} = \mathbf{U}'^{(j)} + \boldsymbol{\Omega}'^{(j)} \times (\mathbf{x} - \mathbf{x}_0)$. Here, $\mathbf{U}'^{(j)}$ and $\boldsymbol{\Omega}'^{(j)}$ are the unknown translational and angular velocities of the particle driven by the external force or the external torque in subproblem j. We note that in the subproblems $j = 1, 2, 4$, and 5, the imposed force or torque [e.g., $F_x'^{(1)}$, below Eq. (A3)] will give rise to additional, off-diagonal forces or torques [e.g., $\tau_y'^{(1)}$, below Eq. (A3)] due to friction from the boundary.

We apply the Lorentz theorem in Eq. (A1) to each of the six pairs obtained by combining the unprimed problem with subproblem j. At the planar wall, $\mathbf{u}'^{(j)}$ vanishes, and far away from the particle, it decays at least as fast as $1/r$. Therefore, concerning the integral over the whole boundary of the fluid domain, only the part over the surface of the particle contributes. The velocity field $\mathbf{u}$ decays at least as fast as $1/r$, and therefore, only the surface of the particle and the wall contribute to the integral involving $\mathbf{u}$. This leads to the following set of equations:

$$\int_{z=0} \mathbf{u} \cdot \boldsymbol{\sigma}'^{(j)} \cdot \hat{\mathbf{z}}\, dS + \int_{|\mathbf{r}|=R} \mathbf{u} \cdot \boldsymbol{\sigma}'^{(j)} \cdot \hat{\mathbf{n}}\, dS = \int_{|\mathbf{r}|=R} \mathbf{u}'^{(j)} \cdot \boldsymbol{\sigma} \cdot \hat{\mathbf{n}}\, dS,\ j = 1, \ldots, 6, \tag{A2}$$

where we have split the lhs into two integrals, $\mathbf{r} \equiv \mathbf{x} - \mathbf{x}_0$, where $\mathbf{x}_0 = (x_p, y_p, h)$ is the center of the particle. Inserting the boundary conditions for $\mathbf{u}'^{(j)}$ and $\mathbf{u}^{(j)}$ into Eq. (A2) and exploiting the fact that the self-propelled particle is force- and torque-free, we obtain six coupled equations

$$\mathbf{U}^{ws} \cdot \mathbf{F}'^{(j)} + \boldsymbol{\Omega}^{ws} \cdot \boldsymbol{\tau}'^{(j)} = -\int_{z=0} \mathbf{v}_s \cdot \boldsymbol{\sigma}'^{(j)} \cdot \hat{\mathbf{z}}\, dS,\ j = 1, \ldots, 6, \tag{A3}$$

where $\mathbf{F}'^{(j)}$ and $\boldsymbol{\tau}'^{(j)}$ are the force and torque, respectively, *from the fluid on the particle* in subproblem j.

In addition to the generalized velocity vector $\mathbf{V}$ introduced above, we also define a generalized force $\mathfrak{F}'^{(j)} \equiv (\mathbf{F}'^{(j)}, \tau'^{(j)})$. In

each subproblem j, the component $\mathfrak{F}_j'^{(j)}$, such as $F_x'^{(1)}$ or $\tau_x'^{(4)}$, must exactly cancel the imposed force or torque because the motion of the particle is overdamped ($Re \ll 1$). It is therefore known *a priori* that, e.g., $F_x'^{(1)} = -F'^{ext}$ and $\tau_x'^{(4)} = -\tau'^{ext}$. The other, off-diagonal components, such as $\tau_y'^{(1)}$, are unknown prior to finding the solution of subproblem j. However, the off-diagonal terms are significant only if the particle is very close to the wall, i.e., if $h/R \approx 1$.[58] We therefore neglect the off-diagonal terms and obtain

$$\mathfrak{F}_j'^{(j)} V_j \approx -\int \mathbf{v}_s \cdot \boldsymbol{\sigma}'^{(j)} \cdot \hat{\mathbf{z}}\, dS,\ j = 1, \ldots, 6, \tag{A4}$$

where V_j are the components of the generalized velocity $\mathbf{V}$. [We note that the left-hand side of Eq. (A4) is not a sum over j.] Due to the linearity of the Stokes equation, $\boldsymbol{\sigma}'^{(j)}$ contains as a prefactor either F'^{ext} or τ'^{ext}, i.e., $-\mathfrak{F}_j'^{(j)}$ Therefore, the arbitrary amplitudes F'^{ext} or τ'^{ext} drop out of the problem. In order to avoid a clumsy notation, in the following, we shall denote $\boldsymbol{\sigma}'^{(j)}/\mathfrak{F}_j'^{(j)}$ as $\boldsymbol{\sigma}'^{(j)}$.

In order to perform the integral in Eq. (A4) analytically, two expressions are needed: one for $\mathbf{v}_s$ and the other for $\boldsymbol{\sigma}'^{(j)}$. For both quantities, we use the "point-particle" approximation in order to obtain analytically tractable expressions. In Appendices B and C, we derive approximate expressions for the surface concentration gradient $c(\mathbf{x}_s)$ and for the primed fluid stresses $\boldsymbol{\sigma}'^{(j)}$. The knowledge of $c(\mathbf{x}_s)$ permits the determination of the phoretic slip boundary conditions $\mathbf{v}_s(\mathbf{x}_s) = -b_w(\mathbf{x}_s)\nabla_{||}c(\mathbf{x}_s)$.

APPENDIX B: AN APPROXIMATION FOR $\sigma'^{(j)}$ AT THE WALL

We obtain an approximate analytical expression for the shear stress $\boldsymbol{\sigma}'^{(j)}$ by using image solutions for a point force or point torque above a planar wall.[59] This approximation neglects the finite size of the particle, i.e., the no slip condition at the particle surface.

For the "primed" problems $j = 1, 2, 3$, we replace the particle by a point force (Stokeslet) pointing into the directions $\hat{x}$, $\hat{y}$, and $\hat{z}$, respectively, located at $\mathbf{x}_0 = (x_p, y_p, h)$ (i.e., the center of the particle) above a planar wall located at $z = 0$. The fluid satisfies incompressibility and the Stokes equations. As shown by Blake,[59] the governing equations and the no-slip condition at the wall can be satisfied by locating a system of images, which consists of a Stokeslet, a force-dipole, and a source-doublet (see Ref. 59), at the point $\mathbf{x}_I = (x_p, y_p, -h)$. For the sake of clarity, we introduce the mapping $(1,2,3,4,5,6) \overset{s}{\to} (x,y,z,x,y,z)$ connecting the indices of the "primed" problem and the corresponding directions of the unit force or torque (see also below), as well as the shorthand notation $s_j := s(j)$ [i.e., $s_1 := s(1) = x$, $s_5 := s(5) = y$, etc.]. The corresponding fluid velocity at an observation point $\mathbf{x} = (x, y, z)$ is given by

$$8\pi\eta\, u_i'^{(j)} = \left(\frac{1}{r} - \frac{1}{X}\right)\delta_{is_j} + \frac{r_i r_{s_j}}{r^3} - \frac{X_i X_{s_j}}{X^3} + 2h\left(\delta_{s_j\alpha}\delta_{\alpha l} - \delta_{s_j z}\delta_{zl}\right) \times \frac{\partial}{\partial X_l}\left[\frac{hX_i}{X^3} - \left(\frac{\delta_{iz}}{X} + \frac{X_i X_z}{X^3}\right)\right], \tag{B1}$$

where $i \in \{x, y, z\}$, $\alpha \in \{x, y\}$, $\mathbf{r} \equiv \mathbf{x} - \mathbf{x}_0$, $\mathbf{X} \equiv \mathbf{x} - \mathbf{x}_I$, $r \equiv |\mathbf{r}|$, $X \equiv |\mathbf{X}|$, and the Einstein convention of summation over repeated indices is used (here and in the following). We note that the first product of Kronecker delta symbols vanishes if either s_j or l takes the value z, while the second such product contributes only if both s_j and l take the value z. Therefore, the index l in the partial derivative with respect to X_l is taken to be x, y, or z. The pressure is given by

$$4\pi\, P'^{(j)} = \frac{r_{s_j}}{r^3} - \frac{X_{s_j}}{X^3} - 2h\left(\delta_{s_j\alpha}\delta_{\alpha l} - \delta_{s_j z}\delta_{zl}\right)\frac{\partial}{\partial X_l}\left(\frac{X_z}{X^3}\right). \tag{B2}$$

(Although pressure is a scalar quantity, s_j appears in the expression for the pressure because its functional form depends on the direction of the point force.) From the velocity and pressure, it follows that the stress tensor

$$\boldsymbol{\sigma}' = -P'\mathbb{1} + \eta\left(\nabla\mathbf{u}' + \nabla\mathbf{u}'^{T}\right) \tag{B3}$$

in the fluid is given by the following expression:

$$\frac{4\pi\eta}{3}\,\sigma_{ik}'^{(j)} = \frac{r_i r_{s_j} r_k}{r^5} - \frac{X_i X_{s_j} X_k}{X^5} - 2h\left(\delta_{s_j\alpha}\delta_{\alpha l} - \delta_{s_j z}\delta_{zl}\right) \times \left(-\frac{h}{X^5}\delta_{ik}X_l + \frac{z}{X^5}\left(X_i\delta_{lk} + X_k\delta_{il}\right) + \frac{X_i X_k}{X^5}\delta_{zl} - \frac{5zX_iX_lX_k}{X^7}\right). \tag{B4}$$

This expression approximately recovers the stress from a sphere dragged by an external point force in the presence of a wall at $z = 0$, although it neglects the finite size of the sphere (represented, concerning hydrodynamics, by a no-slip condition at the surface of the sphere.)

Concerning the substitution into the reciprocal theorem, we are interested in the quantities $\sigma_{iz}'^{(j)}|_{z=0}$, where $i \in \{x, y\}$. These quantities are components of the shear stress evaluated at the wall. We obtain

$$\sigma_{iz}'^{(1)}|_{z=0} = -\frac{3h}{2\pi}\frac{r_i r_x}{r^5}, \tag{B5}$$

$$\sigma_{iz}'^{(2)}|_{z=0} = -\frac{3h}{2\pi}\frac{r_i r_y}{r^5}, \tag{B6}$$

and

$$\sigma_{iz}'^{(3)}|_{z=0} = \frac{3h^2}{2\pi}\frac{r_i}{r^5}. \tag{B7}$$

Now we turn to the "primed problems" $j = 4, 5, 6$. For these three problems, we consider a point torque oriented into the directions $\hat{x}$, $\hat{y}$, and $\hat{z}$, respectively, located at $\mathbf{x}_0$. For a point torque above a planar wall at $z = 0$, Blake found,[59] via the method of images, that the velocity field is

$$8\pi\eta\, u_i'^{(j)} = \epsilon_{is_jk}\left(\frac{r_k}{r^3} - \frac{X_k}{X^3}\right) + 2h\epsilon_{ks_jz}\left(\frac{\delta_{ik}}{X^3} - \frac{3X_iX_k}{X^5}\right) + 6\epsilon_{ks_jz}\frac{X_iX_kX_z}{X^5}, \tag{B8}$$

where $\epsilon_{\alpha\beta\gamma}$ denotes the Levi-Civita symbol (with the convention that its indices are interpreted as $x \to 1$, $y \to 2$, and $z \to 3$), and as mentioned above, summation over repeated indices is employed here and the following. The pressure is[59]

$$P'^{(j)} = -4\eta \frac{\partial}{\partial X_k}\left(\frac{\epsilon_{ks_jz} X_z}{X^3}\right). \tag{B9}$$

By using the definition [Eq. (B3)] for the stress tensor $\boldsymbol{\sigma}'^{(j)}$, we obtain the corresponding matrix elements iz ($i \in \{x, y\}$) evaluated at the wall, which are needed for substitution into the reciprocal theorem

$$\sigma'^{(4)}_{iz}|_{z=0} = -\frac{3}{4\pi}\frac{\delta_{iy}h^2 - r_i r_y}{r^5}, \tag{B10}$$

$$\sigma'^{(5)}_{iz}|_{z=0} = -\frac{3}{4\pi}\frac{\delta_{ix}h^2 - r_i r_x}{r^5}, \tag{B11}$$

and

$$\sigma'^{(6)}_{iz}|_{z=0} = \frac{3h}{4\pi}\frac{\epsilon_{izk} r_k}{r^5}. \tag{B12}$$

APPENDIX C: MULTIPOLE EXPANSION FOR $c(\mathbf{x}_s)$

For a spherical particle with axisymmetric catalyst coverage in *f*ree *s*pace (i.e., far from bounding surfaces), the solute number density can be expanded in terms of Legendre polynomials[14]

$$c^{fs}(r, \theta') = c_\infty + \frac{R}{D}\sum_{l=0}^{\infty}\frac{\alpha_l}{l+1}\left(\frac{R}{r}\right)^{l+1} P_l(\cos(\theta')), \tag{C1}$$

where α_l are the multipole coefficients of the surface activity (i.e., areal density per time): $\alpha(\theta') = \sum_{l=0}^{\infty}\alpha_l P_l(\cos(\theta'))$, $\mathbf{r}$ is the vector from the center of the particle to an observation point, $r = |\mathbf{r}|$, and θ' is the angle between $\mathbf{r}$ and the vector $\hat{\mathbf{d}}$ oriented along the axis of symmetry of the particle. As defined in the main text, $\hat{\mathbf{d}}$ points from the catalytic cap of the particle to the inert region. For any specification $\alpha(\theta')$ of the particle activity, the coefficients α_l are easily calculated. For instance, for the constant-flux model of the activity presented in the main text, one has the monopole coefficient $\alpha_0 = \kappa/2$ and the dipole coefficient $\alpha_1 = -3\kappa/4$. (The sign of α_1 is negative due to our choice of the direction of $\hat{\mathbf{d}}$.)

Now we consider an active particle near a planar wall in a configuration in which $\hat{\mathbf{d}}$ is parallel to the wall (which occupies the xy plane); thus, one has $\hat{\mathbf{d}} = (\cos(\phi), \sin(\phi), 0)$. (The conditions, under which such configurations can be realized, are discussed in Refs. 51 and 52.) In order to obtain approximate analytical expressions for the surface gradient $\nabla_{||}c(\mathbf{x}_s)$, we make two approximations: (i) We truncate the multipole expansion for the activity of the particle, and we consider only the monopole and dipole terms. (ii) In order to model the effect of confinement of the solute field by the wall, we place the mirror images of the monopole and the dipole below the wall. We neglect additional reflections of these two images across the particle surface. In Refs. 51 and 52, these assumptions have been validated via comparisons of the theoretically predicted dynamical behavior of the particle with that obtained from numerical solutions of the full problem.

We therefore write $c(\mathbf{x}_s) \approx c^{mp}(\mathbf{x}_s) + c^{dp}(\mathbf{x}_s)$. Here, $c(\mathbf{x}_s)$ is the sum of two terms: the field due to a point source (*mono*pole) of the number density located at the center $\mathbf{x}_0 = (x_p, y_p, h)$ of the particle, plus the field due to an *i*mage point source of the number density located at $\mathbf{x}_I = (x_p, y_p, -h)$. The second term, $c^{dp}(\mathbf{x}_s)$, is a contribution from a *dip*ole and its image. The real and image dipoles are likewise located at $\mathbf{x}_0$ and at the image point $\mathbf{x}_I$, respectively, and both have the strength $\mathbf{p} = -|\alpha_1|\hat{\mathbf{d}}$.

For the monopole term, we obtain

$$c^{mp}(\mathbf{x}_s) = \frac{2\alpha_0 R^2}{Dr} \tag{C2}$$

and

$$\nabla_{||}c^{mp}(\mathbf{x}_s) = -\frac{2\alpha_0 R^2 \mathbf{r}_s}{Dr^3}. \tag{C3}$$

Here, $\mathbf{x}_s = (x, y, 0)$ denotes a point at the wall, $\mathbf{r}_s = (x - x_p, y - y_p, 0)$ and $r = \sqrt{(x-x_p)^2 + (y-y_p)^2 + h^2}$. For the dipole term, we obtain

$$c^{dp}(\mathbf{x}_s) = -\frac{|\alpha_1|R^3}{D}\frac{\hat{\mathbf{d}}\cdot\mathbf{r}_s}{r^3} \tag{C4}$$

and

$$\nabla_{||}c^{dp}(\mathbf{x}_s) = -\frac{|\alpha_1|R^3}{Dr^3}\left(\mathbb{1} - \frac{3\mathbf{r}_s\otimes\mathbf{r}_s}{r^2}\right)\cdot\hat{\mathbf{d}}. \tag{C5}$$

More details concerning the calculation of the chemiosmotic contribution to the linear and angular velocities of the particle, as well as a discussion of the effect of the nonvanishing size of the particle, can be found in the supplementary material of Ref. 51.

APPENDIX D: EVENNESS OF $U_x^{mp}(x_p)$ FOR CHEMICAL STEPS

We provide here a general symmetry argument according to which $U_x^{mp}(x_p)$ for a chemical step is mirror symmetric with respect to $x_p = 0$ [see Eq. (12)]. By linearity, we can express the monopolar contribution to the velocity as

$$U_x^{mp}(x_p) = b_w^r g^r(x_p) + b_w^l g^l(x_p) + C. \tag{D1}$$

Without osmotic response ($b_w^r = 0$ and $b_w^l = 0$), one has $U_x^{mp} = 0$, and therefore, $C = 0$. Furthermore, we know that $U_x^{mp}(x_p) = 0$ for a uniform wall, i.e., if $b_w^r = b_w^l$,

$$g^l(x_p) = -g^r(x_p) \tag{D2}$$

and

$$U_x^{mp}(x_p) = (b_w^r - b_w^l)g^r(x_p). \tag{D3}$$

Additionally, the mirror symmetry about $x = 0$ requires that $g^l(x_p) = -g^r(-x_p)$ (see Fig. 14). When this result is combined with Eq. (D2), it yields that $g^r(x_p)$ is even

$$g^r(x_p) = g^r(-x_p). \tag{D4}$$

Applying the mirror symmetry (i.e., the parity) operator with respect to the y-axis one obtains $b_w^l \to b_w^r$, $b_w^r \to b_w^l$, $x_p \to -x_p$, and $U_x^{mp}(x_p) \to -U_x^{mp}(-x_p)$ so that

$$-U_x^{mp}(-x_p) = -(b_w^r - b_w^l)g^r(-x_p). \tag{D5}$$

Consequently,

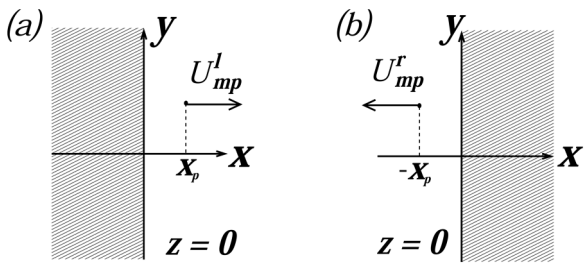

FIG. 14. (a) Schematic illustration of the contribution $U^l_{mp} = b_w g^l(x_p)$ of the left-hand side of the substrate surface $z = 0$ (shaded area) to the translational velocity of a particle at $x = x_p$ for $b^l_w \equiv b_w$. This contribution can be calculated by taking $b^r_w = 0$ on the right-hand side of the substrate surface (white area). U^l_{mp} can be either positive or negative; here, $U^l_{mp} > 0$ is chosen for illustration. (b) Upon applying a mirror transformation about $x = 0$ to (a), we find that the resulting contribution has changed sign. However, panel (b) also illustrates the contribution $U^r_{mp} = b_w g^r(-x_p)$ to the translational velocity of a particle at $x = -x_p$ from the right-hand side of the substrate surface (shaded area) for $b^r_w = b_w$. Accordingly, the relation $g^l(x_p) = -g^r(-x_p)$ holds.

$$U_x^{mp}(-x_p) = (b_w^r - b_w^l) g^r(-x_p) \tag{D6}$$

or

$$U_x^{mp}(-x_p) = U_x^{mp}(x_p), \tag{D7}$$

where we have used Eq. (D4). We conclude that $U_x^{mp}(x_p)$ is an even function of x_p, and, for a given distance from the step, does not depend on whether the particle is to the left or to the right of the step.

REFERENCES

[1] W. F. Paxton, K. C. Kistler, C. C. Olmeda, A. Sen, S. K. St. Angelo, Y. Y. Cao, T. E. Mallouk, P. E. Lammert, and V. H. Crespi, J. Am. Chem. Soc. **126**, 13424 (2004).
[2] W. F. Paxton, S. Sundararajan, T. E. Mallouk, and A. Sen, Angew. Chem., Int. Ed. **45**, 5420 (2006).
[3] W. F. Paxton, P. T. Baker, T. R. Kline, Y. Wang, T. E. Mallouk, and A. Sen, J. Am. Chem. Soc. **128**, 14881 (2006).
[4] S. J. Ebbens and J. R. Howse, Soft Matter **6**, 726 (2010).
[5] M. N. Popescu, W. E. Uspal, and S. Dietrich, Eur. Phys. J.: Spec. Top. **225**, 2189 (2016).
[6] P. Illien, R. Golestanian, and A. Sen, Chem. Soc. Rev. **46**, 5508 (2017).
[7] J. L. Moran and J. D. Posner, Annu. Rev. Fluid Mech. **49**, 511 (2017).
[8] L. Baraban, D. Makarov, R. Streubel, I. Mönch, D. Grimm, S. Sánchez, and O. G. Schmidt, ACS Nano **6**, 3383 (2012).
[9] W. Wang, W. Duan, S. Ahmed, T. E. Mallouk, and A. Sen, Nano Today **8**, 531 (2013).
[10] S. Sánchez, L. Soler, and J. Katuri, Angew. Chem., Int. Ed. **54**, 1414 (2015).
[11] S. Palagi and P. Fischer, Nat. Rev. Mater. **3**, 113 (2018).
[12] R. Golestanian, T. B. Liverpool, and A. Ajdari, Phys. Rev. Lett. **94**, 220801 (2005).
[13] J. R. Howse, R. A. L. Jones, A. J. Ryan, T. Gough, R. Vafabakhsh, and R. Golestanian, Phys. Rev. Lett. **99**, 048102 (2007).
[14] R. Golestanian, T. B. Liverpool, and A. Ajdari, New J. Phys. **9**, 126 (2007).
[15] H.-R. Jiang, N. Yoshinaga, and M. Sano, Phys. Rev. Lett. **105**, 268302 (2010).
[16] J. L. Moran and J. D. Posner, J. Fluid Mech. **680**, 31 (2011).
[17] J. M. Catchmark, S. Subramanian, and A. Sen, Small **1**, 202 (2005).
[18] M. N. Popescu, S. Dietrich, M. Tasinkevych, and J. Ralston, Eur. Phys. J. E **31**, 351 (2010).
[19] S. Ebbens, D. A. Gregory, G. Dunderdale, J. R. Howse, Y. Ibrahim, T. B. Liverpool, and R. Golestanian, Europhys. Lett. **106**, 58003 (2014).
[20] A. Brown and W. Poon, Soft Matter **10**, 4016 (2014).
[21] A. T. Brown, W. C. Poon, C. Holm, and J. De Graaf, Soft Matter **13**, 1200 (2017).
[22] I. Buttinoni, G. Volpe, F. Kümmel, G. Volpe, and C. Bechinger, J. Phys.: Condens. Matter **24**, 284129 (2012).
[23] A. Würger, Phys. Rev. Lett. **115**, 188304 (2015).
[24] S. Samin and R. van Roij, Phys. Rev. Lett. **115**, 188305 (2015).
[25] A. Erbe, M. Zientara, L. Baraban, C. Kreidler, and P. Leiderer, J. Phys.: Condens. Matter **20**, 404215 (2008).
[26] L. Baraban, M. Tasinkevych, M. N. Popescu, S. Sánchez, S. Dietrich, and O. G. Schmidt, Soft Matter **8**, 48 (2012).
[27] G. Rückner and R. Kapral, Phys. Rev. Lett. **98**, 150603 (2007).
[28] Y.-G. Tao and R. Kapral, J. Chem. Phys. **128**, 164518 (2008).
[29] Y.-G. Tao and R. Kapral, Soft Matter **6**, 756 (2010).
[30] M.-J. Huang, J. Schofield, and R. Kapral, Soft Matter **12**, 5581 (2016).
[31] M.-J. Huang, J. Schofield, and R. Kapral, New J. Phys. **19**, 125003 (2017).
[32] B. V. Derjaguin, G. P. Sidorenkov, E. A. Zubashchenkov, and E. V. Kiseleva, Kolloidn. Zh. **9**, 335 (1947).
[33] J. L. Anderson, Annu. Rev. Fluid Mech. **21**, 61 (1989).
[34] S. Michelin and E. Lauga, Eur. Phys. J. E **38**, 7 (2015).
[35] M. Lisicki, S. Y. Reigh, and E. Lauga, Soft Matter **14**, 3304 (2018).
[36] Y. Ibrahim, R. Golestanian, and T. B. Liverpool, Phys. Rev. Fluids **3**, 033101 (2018).
[37] M. Tătulea-Codrean and E. Lauga, J. Fluid Mech. **856**, 921 (2018).
[38] M. N. Popescu, W. E. Uspal, C. Bechinger, and P. Fischer, Nano Lett. **18**, 5345 (2018).
[39] M. N. Popescu, M. Tasinkevych, and S. Dietrich, Europhys. Lett. **95**, 28004 (2011).
[40] M. N. Popescu, S. Dietrich, and G. Oshanin, J. Chem. Phys. **130**, 194702 (2009).
[41] F. Yang, S. Qian, Y. Zhao, and R. Qiao, Langmuir **32**, 5580 (2016).
[42] G. Volpe, I. Buttinoni, D. Vogt, H. J. Kummerer, and C. Bechinger, Soft Matter **7**, 8810 (2011).
[43] S. Spagnolie and E. Lauga, J. Fluid Mech. **700**, 105 (2012).
[44] K. Ishimoto and E. A. Gaffney, Phys. Rev. E **88**, 062702 (2013).
[45] W. E. Uspal, M. N. Popescu, S. Dietrich, and M. Tasinkevych, Soft Matter **11**, 434 (2015).
[46] J. Simmchen, J. Katuri, W. E. Uspal, M. N. Popescu, M. Tasinkevych, and S. Sánchez, Nat. Commun. **7**, 10598 (2016).
[47] S. Das, A. Garg, A. I. Campbell, J. Howse, A. Sen, D. Velegol, R. Golestanian, and S. J. Ebbens, Nat. Commun. **6**, 8999 (2015).
[48] A. Mozaffari, N. Sharifi-Mood, J. Koplik, and C. Maldarelli, Phys. Fluids **28**, 053107 (2016).
[49] Y. Ibrahim and T. B. Liverpool, Eur. Phys. J.: Spec. Top. **225**, 1843 (2016).
[50] A. Mozaffari, N. Sharifi-Mood, J. Koplik, and C. Maldarelli, Phys. Rev. Fluids **3**, 014104 (2018).
[51] W. E. Uspal, M. N. Popescu, S. Dietrich, and M. Tasinkevych, Phys. Rev. Lett. **117**, 048002 (2016).
[52] W. E. Uspal, M. N. Popescu, M. Tasinkevych, and S. Dietrich, New J. Phys. **20**, 015013 (2018).
[53] J.-X. Chen, Y.-G. Chen, and R. Kapral, Adv. Sci. **5**, 1800028 (2018).
[54] W. F. Paxton, A. Sen, and T. E. Mallouk, Chem.–Eur. J. **11**, 6462 (2005).
[55] J. Happel and H. Brenner, *Low Reynolds Number Hydrodynamics* (Prentice-Hall, Englewood Cliffs, NJ, 1965).
[56] J. Loehr, D. Pfeiffer, D. Schüler, and T. M. Fischer, Soft Matter **12**, 3631 (2016).
[57] A. Nourhani, D. Brown, N. Pletzer, and J. G. Gibbs, Adv. Mater. **29**, 1703910 (2017).
[58] A. Goldman, R. Cox, and H. Brenner, Chem. Eng. Sci. **22**, 637 (1967).
[59] J. R. Blake and A. T. Chwang, J. Eng. Math. **8**, 23 (1974).